



Effect of Cu^{2+} on deposition mechanism and structure of ZrO_2 -based conversion coatings on AA6060 aluminium alloys and their susceptibility to filiform corrosion

Erlind Mysliu^a, Kathrine Sletteberg Storli^a, Hanna Marie Skogøy^a, Stephan Kubowicz^b, Ingeborg-Helene Svenum^c, Otto Lunder^c, Andreas Erbe^{a,*}

^a NTNU, Norwegian University of Science and Technology, 7491 Trondheim, Norway

^b SINTEF Industry, Pb. 124 Blindern, 0314 Oslo, Norway

^c SINTEF Industry, 7465 Trondheim, Norway

ARTICLE INFO

Dataset link: <https://doi.org/10.18710/DYRRAE>

Keywords:

Recycled aluminium
Conversion coating
Pretreatment
Filiform corrosion
Zirconium oxide

ABSTRACT

Zirconium oxide-based conversion coatings (CCs) were prepared from hexafluorozirconic acid, H_2ZrF_6 , with and without Cu^{II} as an additive. The CCs were prepared on primary and recycled AA6060. The deposition mechanism, structure, electrochemical properties and effectiveness in protection against filiform corrosion (FFC) have been explored. In presence of Cu^{II} additives, a two step deposition mechanism is observed, evidenced by open circuit potential measurements and in situ dynamic electrochemical impedance spectroscopy. Copper deposits predominantly as copper(II) hydroxyfluoride on the top surface, and metallic Cu^0 at the metal/CC interface, as evidenced by x-ray photoelectron spectroscopy and glow-discharge optical emission spectroscopy. The presence of a Cu^{II} additive induces a different distribution of the ZrO_2 -based products. After deposition of a weak organic model coating, aluminium pretreated with the Cu^{II} -containing system shows a 10%–30% lower maximum filament length compared to the Cu^{II} -free system in FFC tests, despite a ca. one order of magnitude higher cathodic activity of the former.

1. Introduction

Recycling of aluminium has a huge economic and environmental impact, as production of recycled aluminium reduces energy consumption and CO_2 emissions compared to the production of primary alloys [1]. For this reason there is strong interest in aluminium recycling — from policy to technology development. Efficient scrap sorting technologies allow for good control over the composition of the resulting recycled alloy [2]. However, in some cases, an enrichment of elements such as Fe, Mn, Si, Cu, and Zn can occur. In general in aluminium alloys, the formation of noble intermetallic particles (IMPs), especially Cu or Al(Mn,Fe,Si)-based particles, can in corrosive environments lead to the formation of microgalvanic cells, increasing the susceptibility towards localised corrosion [3].

Filiform corrosion (FFC) can under certain environmental conditions, such as the presence of chloride and coatings defects, be initiated on painted aluminium usually employed in the automotive and building industry. FFC has a rather complex mechanism involving several cathodic reactions and successive pitting formation with start-stop cycles [4]. The susceptibility to this surficial localised corrosion

process has been found to be strongly dependent on the sample's thermomechanical history, as FFC susceptibility is affected by surface microstructure, texture, and composition [5–7]. Especially, the presence of more noble elements included in IMPs in the near-surface region increases susceptibility to FFC [8]. Alkaline etching and acidic desmutting increase resistance to FFC by removing the surface active layer produced during thermomechanical treatment [5,9].

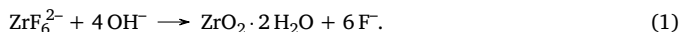
Conversion coatings (CCs) are used to further decrease the FFC susceptibility by reducing the potential difference between metal matrix and IMPs [10], by forming a physical barrier [11], or by providing a better adhesion for organic coatings [12–14]. Chromate-based CCs have been proven to be very effective in protecting against FFC [12], however, due to the toxicity of Cr^{VI} , alternatives have been developed. Such alternatives include ZrO_2 or TiO_2 based CCs [15,16], silicon alkoxide derived sol-gels [17,18], their hybrids [19,20], and layered double hydroxides [21]. Some of the most important CCs applied on an industrial scale are those based on TiO_2 and ZrO_2 [22]. Several aspects of the deposition mechanism have been studied [10,15,23–27].

* Corresponding author.

E-mail address: cc-recycled-al@the-passivists.org (A. Erbe).

In addition to its contribution to corrosion protection, ZrO_2 is also self-cleaning [28].

The CC deposition mechanism, its resulting surface morphology and its composition depend on the composition of the aluminium substrate [29]. In general, the catalytic activity of noble IMPs towards the oxygen reduction reaction (ORR) and hydrogen evolution reaction (HER) increases local alkalinity [30], thus favouring the deposition of the conversion film by the net reaction



The corrosion resistance of immersed aluminium alloys coated with ZrO_2 -based CCs is increased by the formation of a multilayered structure due to the precipitation of compact $ZrO_2(H_2O)_2$ and $Al(OH)_3$ which is deposited on the top layer [31,32]. A certain immersion time was found to be required for the formation of a conversion layer which ensures optimal corrosion protection [33]. On Zn/Al metallic coatings on steel, the final CC consists of a complex mixture of different oxides, including aluminium oxide, and fluorides [27]. Fast, impedance-based electrochemical in situ experiments have very recently yielded more detailed insight into the CC formation processes on galvanised steel [34].

An important way of accelerating ZrO_2 deposition is the addition of Cu^{II} to the bath [24]. This additive is also commonly applied in industrial coatings, e.g. [22]. The Cu^{II} can precipitate on the aluminium surface as metallic Cu or as CuO [35,36] based on a mechanism proposed by Andreatta et al. [10]. Surfaces enriching in noble IMPs favour the deposition of the conversion film following net reaction (1) and modify the structure of the formed surface layer [26]. Auger electron spectroscopy revealed the presence of a mixture of ZrO_2 , zirconium oxyhydroxides and oxyfluorides precipitated on the top of Cu^0 particles [35]. However, the internal structure of the formed conversion film is likely more complex. A mixture of Cu-based and ZrO_2 -based compounds has been observed on Fe substrates [37] after the deposition of a ZrO_2 -based CC in presence of Cu^{II} additives. Zones of the conversion film rich in Cu have been observed also on aluminium substrates [38]. The thickness of the ZrO_2 -based compounds deposited on aluminium surfaces from conversion baths based on hexafluorozirconic acid containing Cu additives is influenced by the preparation of the surface prior to the immersion in the conversion bath [39]. The alloy composition is also important: in Cu containing aluminium alloys such as AA6014, the distribution of Cu-based products – which influences the distribution and thickness of ZrO_2 -based products – is different compared to AA1050 [39].

Increasing initial hydroxyl group density on an aluminium surface also enhances deposition of ZrO_2 [40]. Combination of Cu^{II} with oxidising NO_3^- yields additional enhancement of deposition [36]. Other ionic additives such as Ce^{3+} [41] can further fine-tune properties of this class of CCs. On the other hand, the presence of Cu in the alloy does not increase deposition rates very much but contributes to adhesion [42]. The difference in alloy composition is also reflected by the protection efficiency against corrosion. The same ZrO_2 -based CC could be efficient in decreasing corrosion rates of AA3005 and AA5754 aluminium alloys while it can have no effect on AA2024 and AA7075 due to a negative effect of Cu and Zn rich intermetallic particles [29]. The effect of Cu in the conversion coating bath on corrosion resistance is overall controversial. Both beneficial [24] and negative [43,44] effects of Cu on corrosion protection have been reported. ZrO_2 -based CCs themselves are very stable under cathodic polarisation, which is important for application in cathodic electrodeposition coatings [45].

Silane-containing fluorotitanate conversion coatings were found to have a bilayer structure with the silane film laying on top of the TiO_2 . This structure was deduced from a difference of 10 nm between the peak maxima for Si and Ti found by glow discharge optical emission spectroscopy (GD-OES) depth profiling [43]. Bifunctional silanes are beneficial for organic coating adhesion [18,46–48]. Also typical electrochemical parameters such as corrosion current density suggest a lower

Table 1

Elemental composition, in mass-% of Ni8, R (primary based) and C3 (based on >75% post-consumer scrap). Sample Ni8 was part of a series with systematically varied Ni content and used here only for ToF-SIMS characterisation. Balance Al.

Element	C3	R	Ni8
Si	0.50	0.4382	0.438
Fe	0.2142	0.1722	0.207
Cu	0.0307	0.0027	0.0010
Mn	0.0439	0.0481	0.0490
Mg	0.3584	0.3840	0.357
Cr	0.0078	0.0001	0.0007
Ni	0.061	0.0034	0.0459
Zn	0.032	0.0052	0.0003
Ti	0.06	0.0165	0.0092
Pb	0.0028	0.0007	0.0010

short term corrosion rate in the presence of additives [49]. Polymeric additives in ZrO_2 -based CCs affect the distribution of Cu and voids on iron [37]. Polymeric additives are incorporated into CCs on different substrates [50,51], and improve stability of polymeric/metal interfaces [52]. CC protection is affected by exact precursor choice [53]. ZrO_2 is also a component in trivalent chromium CCs and important for their deposition [54].

Pretreatment steps such as alkaline etching [55], and desmutting [26,56], applied before CCs crucially affect the CC deposition because they affect electrochemical properties of surfaces via modification of surface composition of both metal matrix and IMPs. The efficiency of the CC deposition and its protection against corrosion is affected by the substrate composition; a system optimised for a certain aluminium alloy [57] could yield different performance on another [58] even if the surface preparation is identical.

This work aims to investigate the deposition mechanism and resulting structure of ZrO_2 -based CCs deposited in the presence of a Cu^{II} additive, and the consequences for FFC rates on two extruded AA6060-T6 aluminium alloys. One of the systems is based on more than 75% post-consumer scrap. The other is a primary-based alloy with a lower content of Cu and Zn. Two ZrO_2 -based conversion systems are investigated. A conversion bath containing a Cu^{II} additive is compared with a bath of pure aqueous H_2ZrF_6 . Insight into the CC deposition mechanism was obtained in situ by open circuit potential (OCP) measurements and dynamic electrochemical impedance spectroscopy (dEIS). Samples with CCs were characterised by GD-OES and X-ray photoelectron spectroscopy (XPS) depth profiling, time-of-flight secondary ion mass spectrometry (ToF-SIMS) as well as scanning electron microscopy (SEM) with energy-dispersive X-ray spectroscopy (EDX). In addition to interpreting data obtained in this work, the literature about the state of the Zr-containing precursors in solution is analysed and discussed as background for the observed film formation. By measurements of cathodic polarisation curves, the cathodic activity of different surfaces was obtained, and set in relation to results from a FFC test with an organic model coating.

2. Materials and methods

2.1. Materials

Two different AA6060-T6 aluminium alloys (composition in Table 1) have been used for the main work, designated as R and C3. The samples differ mainly in the Cu and Zn content which is slightly higher for C3 (which is based on more than 75% of post-consumer scrap). In addition, a sample called Ni8 was included in the for ToF-SIMS characterisation at intermediate deposition stages. The composition of the samples was determined via inductively coupled plasma optical emission spectroscopy by the industrial research and development laboratories of the sample supplier.

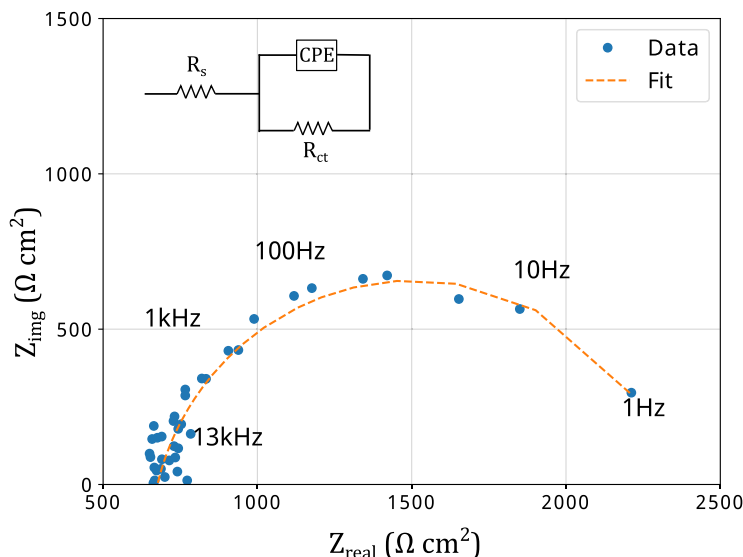


Fig. 1. Example of experimental dEIS spectra and fitting using the impedance.py package. The equivalent circuit used to fit the data is shown as a figure inset. R_s — solution resistance, R_{ct} — charge transfer resistance, CPE — constant phase element.

The samples were cleaned with acetone and ethanol before etching ~ 2 g/m² of the surface by exposure to 10 mass-% aqueous NaOH at 60 °C for 6 s. The smut layer formed during the alkaline etching was removed by acidic desmutting in 96% HNO₃ for 1 min at room temperature. Finally, a ZrO₂-based CC was deposited by immersion of the samples under investigation in a CC bath for 410 s. One of two different conversion systems were used. The first CC was a hexafluorozirconic acid solution that contained <200 mg/L Zr and <50 mg/L Cu to improve the film deposition efficiency [35]. Cu was present in the form of Cu(NO₃)₂. The second CC was an additive-free CC prepared using an amount of H₂ZrF₆ such that the concentration of Zr is 200 mg/L. The two CC systems will be referred to as Cu-CC and model-CC, respectively.

Raw data collected in this study are available via NTNU's institutional repository [59].

2.2. Methods

2.2.1. Electrochemical measurements during CC formation

For all the electrochemical measurements, the working electrode was the sample under investigation, the counter electrode was a platinum foil and the reference electrode was a Ag|AgCl|KCl (sat.) electrode from Hach Lange Sensors. All electrode potentials in this work are given with respect to Ag|AgCl|KCl (sat.). OCP measurements were performed during the CC application.

DEIS was used to study the deposition mechanism of the Cu containing conversion coating. DEIS allows for the combination of conventional electrochemical techniques such as chronoamperometry and cyclic voltammetry with EIS. A DC signal was generated using a Model 175 Universal Programmer and the AC signal was generated using a home-made software described in [60]. The two signals were combined using a SRS SIM900 mainframe with SIM910, SIM980, SIM983 modules and Keithley KUSB-3116 ADC/DAC converter. A Gamry Reference 600 potentiostat was used to apply the signal to the cell. The Keithley KUSB-3116 module was used to continuously sample the current response along with the DC and AC potentials applied to the cell. The frequencies included in the excitation signal were in the range 13 kHz–1 Hz. The excitation frequencies were chosen following the method proposed in Ref. [61]: (i) each frequency is a multiple of the minimum frequency at 13 frequencies per decade, 45 frequencies between 1 Hz–13 kHz; (ii) the rms amplitude for the individual sine waves is decreased by one-half for every decade increase in the frequency; (iii) the phases of

the individual waves were randomised; (iv) the maximum amplitude of the AC waveform was 30 mV which corresponded to a maximum amplitude of 4.5 mV_{rms} for the lowest frequency and a minimum of 0.5 mV_{rms} for the highest frequency. Fast Fourier transform of the output signal allowed the reduction of the acquisition time for an impedance spectrum to 1 s. The short acquisition time allows to overcome the problem of the system stability required during EIS measurements and allows to study fast changing processes [60]. The home-made set-up used for this experiment has been described thoroughly elsewhere [60].

The dEIS spectra were acquired in two different modes. In both modes, the samples were initially left 25 s at OCP. The first mode consisted of potentiodynamic dEIS measurements, sweeping the potential following the natural evolution of the OCP (c.f. Section 3.1) after it reached a minimum. The second mode were potentiostatic measurements where the potential was kept constant at the minimum potential reached by the OCP. Details are given in Section 3.1.

All the impedance spectra were fitted using the impedance.py module in python [62]. Fitting was performed by non-linear least square regression via the “curve_fit” function from the scipy.optimize package [62]. The impedance.py module is convenient when working with several datasets since it enables batch processing. An example of experimental data and fitting is presented in Fig. 1. All spectra can be described well with the equivalent circuit shown in the inset, where R_s represents the solution resistance, R_{ct} represents the charge transfer resistance and a constant phase element (CPE) has been used to model the interfacial capacitance C . R_{ct} contains a contribution from the conversion film resistance although we consider the former to be predominant. C contains contributions from the film capacitance and the double layer capacitance. The extraction of the capacitance value from the CPE has been performed by using the approach suggested by Hsu and Mansfeld [63],

$$C = Q(\omega_c)^{\phi-1} \quad (2)$$

where ϕ and Q are the CPE exponent and prefactor, respectively, while ω_c is the frequency at which the imaginary part of the impedance reaches its maximum value. For the equivalent circuit used here, Eq. (2) can be transformed to [64,65]

$$C = Q^{1/\phi} \left(\frac{1}{R_{ct}} \right)^{1-1/\phi} \quad (3)$$

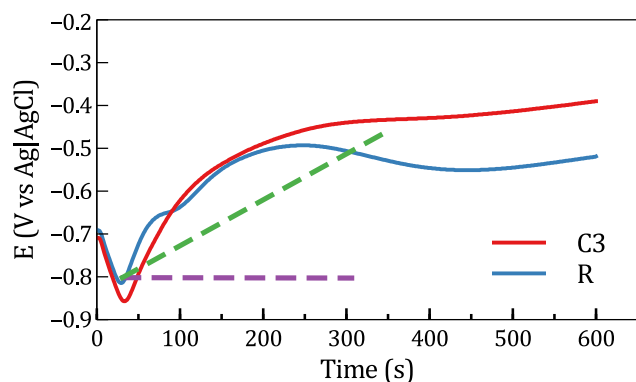


Fig. 2. Full lines: Measured OCP of the two different samples in the Cu-CC bath. Dashed lines: Potential profiles applied during dEIS after 25 s of sample resting at OCP; green: potentiodynamic experiment between 25 s and 350 s; purple: potentiostatic dEIS between 25 s and 310 s.

2.2.2. Corrosion tests and electrochemical properties in NaCl

Potentiodynamic polarisation curves were measured in order to compare the cathodic activity of the surface of the different aluminium samples before and after applying a ZrO₂-based conversion film with and without Cu^{II} additives. A 5 mass-% NaCl solution was used as electrolyte for these measurements. Cathodic polarisation curves were measured starting from OCP, scanning 0.7 V in the negative direction at 0.5 mV/s, using the same electrode configuration as described in Section 2.2.1.

FFC susceptibility was assessed after degreasing, alkaline etching, desmutting and applying the two different ZrO₂-based CCs. The samples were coated with the commercial acrylate-based Paraloid B48 coating (Dow Chemical; supplier Kremer Pigmente) using a spin coater with a program that yielded a ≈ 20 μm thick film. A coating defect was prepared by scratching the surface with an Erichsen Model 639 Corrocutter. FFC was induced by dripping HCl (37%) into the scratch and leaving the system to react for 60 s. The remaining acid was wiped away with laboratory tissue. Finally, the samples were put into a humidity chamber at 40 °C and 86(± 5)% relative humidity and exposed for 1000 h.

2.2.3. Post-mortem characterisation

The surface morphology and composition before and after applying the CCs were analysed by SEM and EDX using a Zeiss - Ultra 55 - FEG-SEM. The acceleration voltage was 15 kV. The number and size of IMPs was estimated using ImageJ [66]. Surface enrichment of different alloying elements was assessed by GD-OES with a Horiba GD-Profilier 2. Quantitative information was obtained after calibration with 12 different standards provided by MBH Analytical, Alcoa, and Alcan.

XPS measurements were performed using a Kratos Axis Ultra instrument equipped with a Al K α source (1486.7 eV). Individual core level regions (Cu 2p, F 1s, C 1s, Zr 3d, Cu 3d, Al 2p), in addition to the Cu LMM Auger region, were acquired using a pass energy of 40 eV. Survey spectra were measured with a pass energy of 160 eV. Depth profiling was performed using Ar-ion sputtering. XPS measurements were first obtained on the as received sample, and after initial sputtering at 0.5 kV for 60 s followed by sputtering cycles at 2 kV. The raw spectra were analysed using CasaXPS.

3. Results

3.1. OCP and dEIS during CC formation

The OCP shown in Fig. 2 during the application of the Cu-CC shows similar features for both R and C3. In the first 30–40 s of exposure,

the potential drops from an initial value of ≈ -700 mV common to both samples to a value of ≈ -800 and ≈ -850 mV for R and C3, respectively. After the initial decay the potential of both samples raises again until reaching a stable value after ≈ 400 s. The maximum potential difference between the two samples is achieved after ≈ 410 s. Therefore, in order to have a higher probability to discriminate between the electrochemical properties of the two surfaces, the two samples were coated for 410 s before further characterisation.

After having immersed sample R for the initial 25 s at OCP, dEIS experiments were conducted with two different potential profiles. Fig. 3 shows the results of the potentiostatic dEIS experiment in which the potential was kept constant near the minimum observed during OCP measurements (dashed purple profile in Fig. 2). In this experiment, the capacitance increased to $\approx 2.5\times$ of its initial value and the CPE exponent decreased from 1 to ≈ 0.8 ; R_{ct} went through a minimum at $\approx 1/3$ of its initial value before stabilising at approximately twice the minimum value.

The R_{ct} measured during the potentiodynamic experiment (Figure S1, Supplementary Material) decreased by 10% during the first ≈ 100 s and raised again after ≈ 200 s to approximately its initial value. The capacitance instead kept decreasing over the whole measurement time, and decreased by $\approx 1/4$.

3.2. Surface characterisation

3.2.1. SEM/EDX

The surface microstructure and composition of R and C3 after the application of Cu-CC or model-CC were analysed by SEM and EDX (Fig. 4; overview in Supplementary Material, Figure S3). In the case of Cu-CC (Fig. 4e–h), the grain boundaries are decorated with elongated IMPs that are much more visible than the particles on the surfaces of samples coated with the model-CC (Figure S3a and b, Supplementary Material). A total particle count shows that the particle density including all particles is higher for C3 than for R especially after applying Cu-CC (Figure S4). For Cu-CC, the biggest difference is caused by the formation of precipitates of a few hundreds of nm in diameter. On alloys manufactured in the same way, the most common particles are α -AlFeSi and α -Al(FeMn)Si [67–70].

Fig. 4 shows a higher magnification SEM image of single IMPs located on the matrix or in the grain boundaries. The results of EDX analyses are compiled in Table 2. In general, in the model-CC, Zr tends to precipitate mainly on the top of usually Fe-rich IMPs. However, a lower amount compared to the top of IMPs was detected on the bare surface as well. After the model-CC was deposited, EDX analyses show that Zr is mainly located on the top of IMPs precipitated in the centre of the grains while the concentration drops on top of the particles located in the grain boundaries. After the Cu-CC conversion coating application, both surfaces are enriched by the presence of bright precipitates (Fig. 4a,b and e,f). Cu is randomly distributed since sometimes its concentration in the proximity of the bright precipitates is high and sometimes is below detection limit. Different from the model-CC, for Cu-CC the highest amount of Zr (and Cu) is found on the top of the IMPs located in the grain boundaries that are Si-rich.

3.2.2. GD-OES

Fig. 5 shows the GD-OES depth profiles of R and C3 after the deposition of the Cu-CC and model-CC. The film thickness can be estimated by the intersection of the Al and O signal [43]. The profile for the two elements is shown in Fig. 5d. In this case, only an approximate film thickness of 50 and 80 nm for model-CC and Cu-CC, respectively, can be extracted because of the lack of standards for the oxygen signal. Nevertheless, the coating deposited from the Cu-CC bath is thicker than that deposited from the model-CC bath which is in agreement with previous works [43,44].

The Cu surface enrichment was similar for both R and C3 after exposure to the Cu-CC bath. After applying the model-CC, only a very

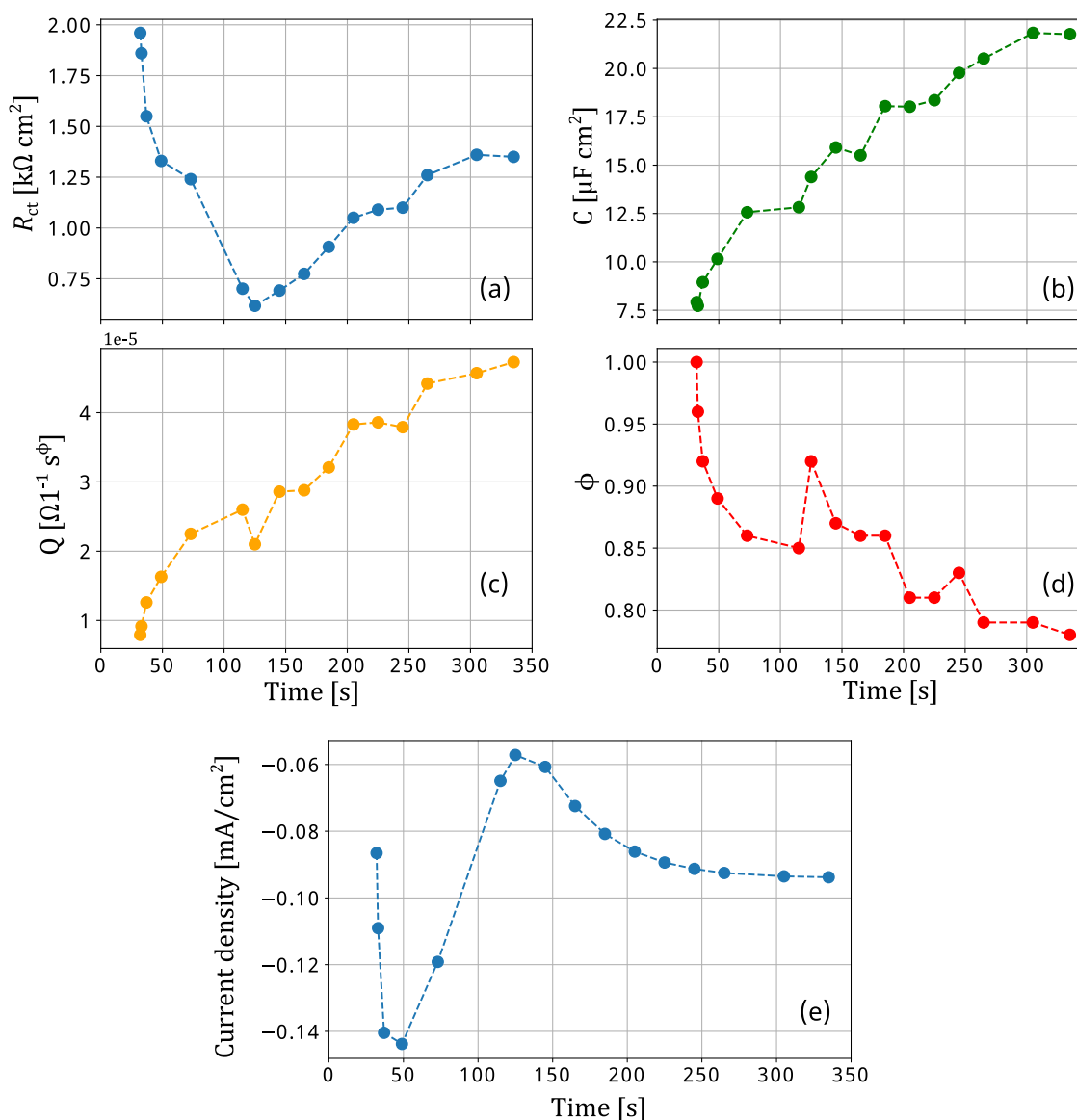


Fig. 3. Electrochemical parameters R_{ct} (a), C (b), Q (c), and ϕ (d) extracted from a potentiostatic dEIS experiment (Nyquist plot c.f. Supplementary Material, Figure S2) of sample R during immersion in Cu-CC bath with potential profile shown by the purple dashed line in Fig. 2. The corresponding current over time is shown in panel (e).

Table 2

Results from EDX analysis of R and C3. All compositions are expressed in mass-%, with typical EDX uncertainties. The letters refers to the picture numbers in Fig. 4 and “GB” indicates particles in grain boundaries.

Elements	a	b	c	d	e (GB)	f (GB)	g (GB)	h (GB)
Al	67.6	66.1	61.7	72.9	54.9	57.1	81.3	85.6
Fe	9.3	18.3	20.4	12.1	–	–	0.2	–
Cu	8.8	–	–	–	19.3	19.2	–	–
Zr	5.8	4.9	6.7	6.2	11.2	11.3	3.6	4.0
O	4.0	3.8	4.3	4.3	8.9	7.5	7.1	4.4
Si	3.5	5.9	6.5	3.9	1.8	1.6	6.7	4.1
Mg	1.0	–	–	–	1.0	1.1	1.2	1.1

small Cu surface enrichment was observed. Cu enrichment is much less pronounced for R (low copper in alloy) than for C3 (high copper in alloy). Analogously, an increase in signal intensity close to the surface is visible also for Fe and Ni (Fig. 5c and d, respectively) which enrich at the surface to a comparable extent for both systems.

The maximum of the surface enrichment of Zr (Fig. 5a) and its position are very similar for both the sample treated with the Cu-CC

and the model-CC. However, the peaks are slightly broader for the Cu-CC reflecting the higher thickness of the deposited film. For Ni, an analogous peak broadening is observed after applying the Cu-CC. Overall, Cu enriches mainly in the outermost part of the surface and the peak maxima are at ≈ 15 nm of depth while Zr, Fe, and Ni tend to have a maximum enrichment at ≈ 40 nm.

3.2.3. XPS

XPS analysis was performed on sample R after applying the Cu-CC. Spectra were measured before sputtering and after different sputtering times (Figs. 6a and b). Before sputtering, the Cu $2p_{3/2}$ region from the surface shows a distinct peak at 932.4 eV binding energy, and a very broad peak with a top ranging from ≈ 935 to ≈ 937 eV (Fig. 6a). The peak at 932.4 eV, which accounts for $\approx 30\%$ of the total intensity, agrees well in position with Cu^0/Cu^1 type species [71]. The distinction between Cu_2O and metallic Cu is in most cases difficult [71], and with this work's data even difficult taking into account the Cu LMM Auger peak (c.f. Supplementary Material, Figure S7). The region 935 to 937 eV comprises peaks of pure $\text{Cu}(\text{OH})_2$ (lower end) and CuF_2 (upper end of the interval) [71]. Satellite peaks as typical for CuF_2 and

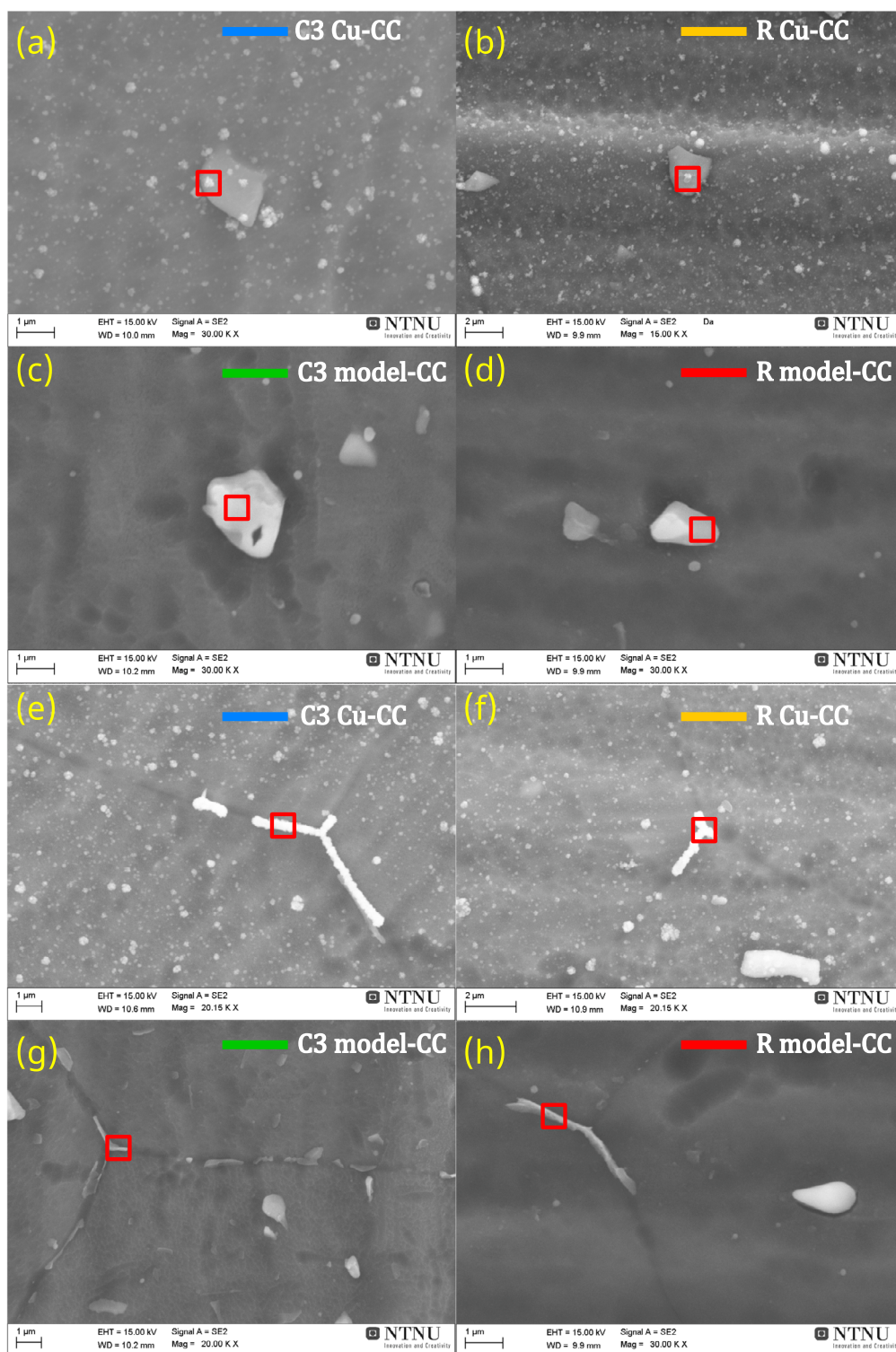


Fig. 4. Detailed SEM images of the surface of R (b, d, f, h) and C3 (a, c, e, g) after Cu-CC (a, b, e, f) and model-CC (c, d, g, h) conversion coating. Overview images c.f. Figure S3, Supplementary Material. The red squares show the position of selected EDX analyses (Table 2). The small green dots represent other EDX measuring sites not described in detail, but used to select representative points compiled in Table 2.

$\text{Cu}(\text{OH})_2$ have been detected in the region 941–950 eV in accordance with literature data [71]. We interpret this result as an indication of the presence of copper hydroxyfluorides, which does contain regions in which Cu^{I} is in a CuF_2 -like environment, regions in which Cu^{II} is in an $\text{Cu}(\text{OH})_2$ -like environment, and different intermediate environments in between those two extremes.

The situation after the first sputtering step is more complex and the assignment of species worth a short discussion. The presence of three components can be observed for the first four measurements in Fig. 6b, whereas only two components remain after the fourth measurement. According to reference data compilations [71,72] the peak positions at ≈ 935 , 933.4, and 932.6 eV agree with those of $\text{Cu}(\text{OH})_2$, CuO , and Cu_2O or Cu , respectively. Following this reasoning, in our case, the

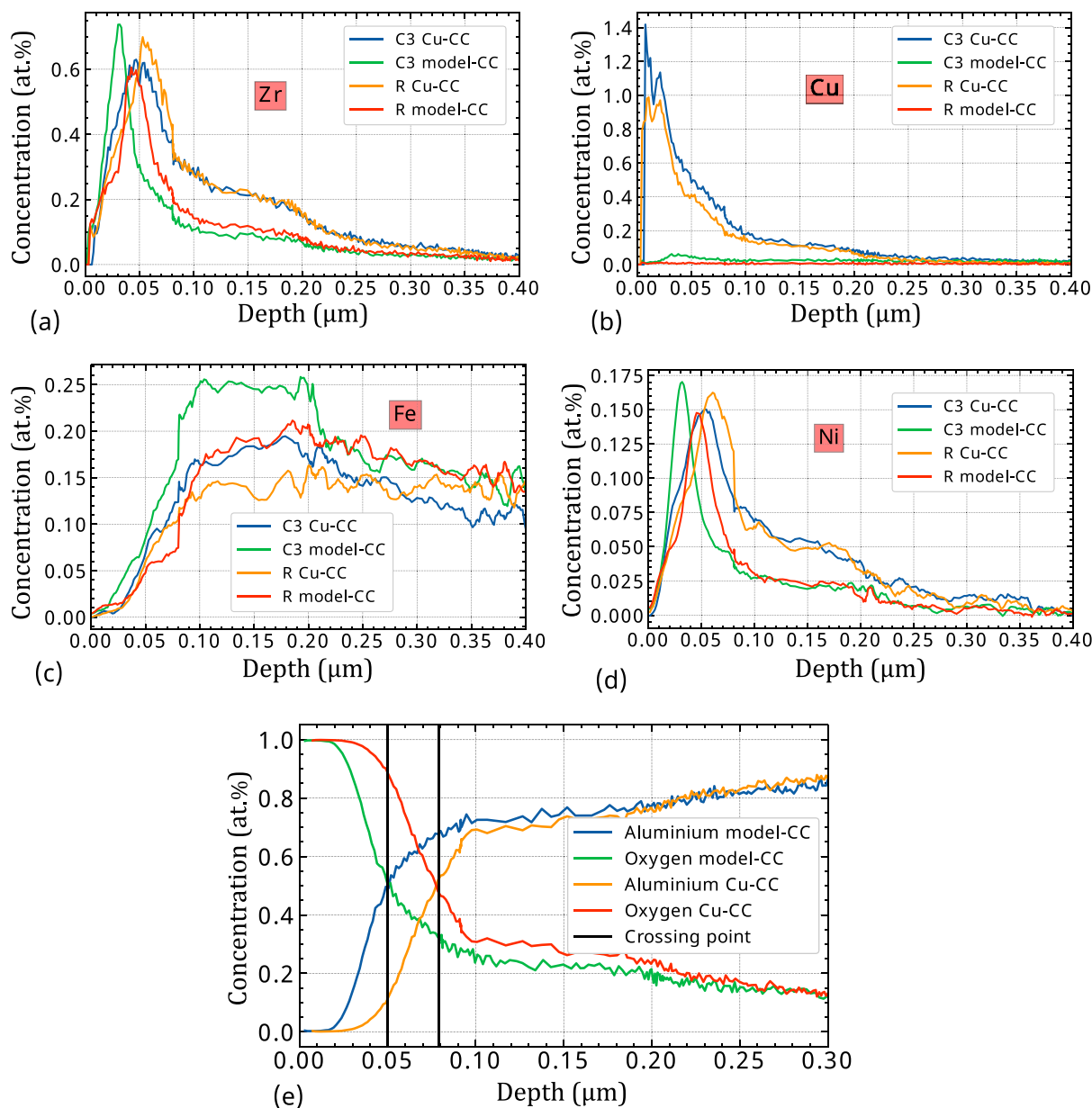


Fig. 5. (a–d) GD-OES elemental profiles of (a) Zr, (b) Cu, (c) Fe and (d) Ni for R and C3 after deposition of the Cu-CC and model-CC for 410 s. (e) Aluminium and oxygen profile of a model-CC and a Cu-CC; the intersections of the Al and O lines are indicated by black vertical lines and used to extract the oxide film thickness.

Cu surface distribution would be characterised by the presence of a layer of copper hydroxyfluorides [composition ranging from $\text{Cu}(\text{OH})_2$ to CuF_2] in the very top surface and a mixture of copper oxyhydroxides (composition involving local motifs of $\text{Cu}(\text{OH})_2$, CuO , and Cu_2O or Cu) for the next four measurements. Only a mixture of CuO and Cu_2O or Cu is observed for the final remaining measurements.

Against this interpretation speaks the fact that both $\text{Cu}(\text{OH})_2$ and CuO show in reference works strong and characteristic satellite peaks (smaller for $\text{Cu}(\text{OH})_2$ [71]) in the region 945–940 eV. These satellite peaks are absent in our spectra. A slight increase in background between 940 and 950 eV is detected in the spectra in Fig. 6b which could hint to the presence of such satellite peaks although the intensity is so low that the presence of any peak cannot be confirmed from the data presented here. A similar assignment of the peak at 933.4 eV to CuO , despite the absence of any satellite peak, has recently been published on a similar system [37]. This interpretation is also consistent with the Cu LMM Auger peak (c.f. Supplementary Material, Figure S6 and S7), where after short sputtering steps, components with the peak energies

of CuO (kinetic energy 917.7 eV) and metallic Cu (918.4 eV) can be clearly distinguished. In the Cu LMM peak, the typical Cu_2O component at 916.8 eV must at best be shifted by almost 1 eV. There are also other features in this peak which are hard to fit. In the satellite peaks, ligand states play an important role [73], and in the strongly disordered system such as thin metal oxide films often are, the distribution of ligand-ion distances may smear out the satellite peaks. Interaction with defects could also account for the observed effects in the traditional interpretation of the satellite peaks in copper oxides, e.g. [74].

An alternative interpretation could be that the peak at ≈ 935 eV is caused by the presence of $\text{Cu}(\text{OH})_2$ type species with a very small satellite peak, the peak at 933.4 eV could be assigned to Cu_2O species and the peak at 932.6 eV to metallic Cu. In this case however the peak position of Cu_2O would be shifted by ≈ 1.6 eV with respect to literature values compiled in Ref. [71]. A slightly different value could be expected in this case since reference values are usually measured on Cu reference samples which have a much less complex composition than in this work. The chemical environment surrounding Cu atoms or

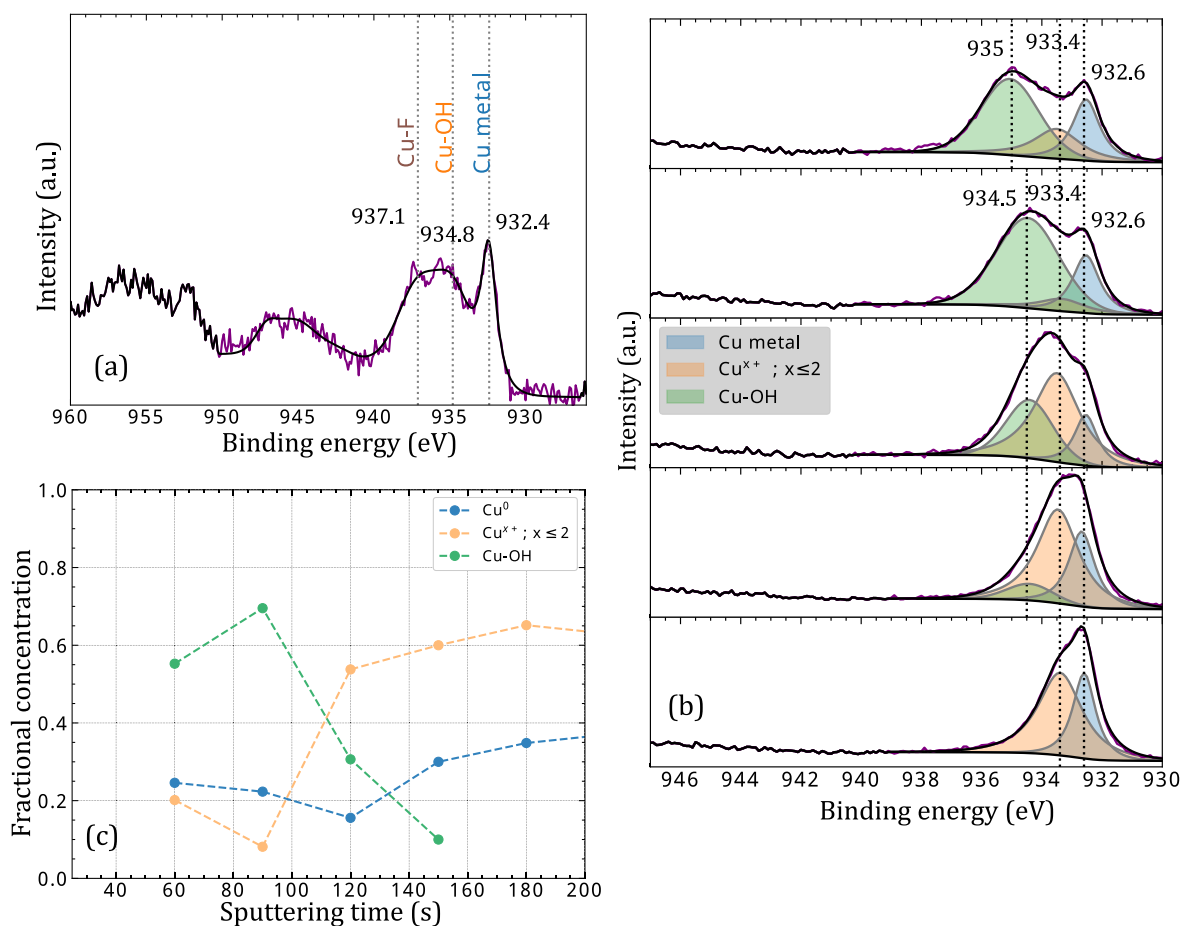


Fig. 6. XPS analysis of sample R after Cu-CC. (a) Cu 2p_{3/2} region at surface without sputtering. Numbers indicate the peak position from Ref. [71] of the component indicated by the dotted line. (b) Cu 2p_{3/2} region after 60, 90, 120, 150 and 180 s of sputtering (top to bottom); the initial 60 s sputtering was only a very mild sputtering step with 0.5 instead of 2 kV acceleration voltage as used for the remaining steps. (c) Concentration profile of different Cu species after different sputtering times as extrapolated from the fitting shown in panels (a) and (b); sum of all Cu species normalised to 1.

Cu-based IMPs would have an effect on the electron's binding energy. It is not intuitively obvious how to explain a shift of the observed magnitude in this system. Another alternative interpretation could be the presence of the mixed copper oxide, Cu₄O₃, e.g. [75], or the presence of substoichiometric oxides. Structural disorder such as vacancies and amorphous fractions in the oxides also affects the exact peak position.

A complete, thorough interpretation of the XPS spectra presented here goes beyond the scope of this work. What is important for the purpose of this work is to highlight the presence of oxidised Cu species as copper hydroxofluorides at the very top surface which change to a form with lower oxidation state deeper in the ZrO₂-based conversion layer. Based on the peak areas shown in Figs. 6a and 6b, a concentration profile of the different Cu species has been established (Fig. 6c). To that end, however, Cu is also known to reduce during sputtering or during exposure of the beam, which is why some aspects of this analysis may be artefacts from the measurement.

3.3. Electrochemical properties and FFC resistance

Cathodic polarisation curves in 5 mass-% NaCl are shown in Fig. 7. The goal of recording these curves was to compare the cathodic activity of the different samples in the same solution. Before applying any conversion coating, corrosion potential E_{corr} and cathodic activity of R are lower than of C3 (red and blue curves in Fig. 2a, respectively). After applying the model-CC the activity of R remains almost unchanged while for C3, a reduction of E_{corr} is observed; cathodic current densities are, however, similar for both samples. After the application of Cu-CC,

both R and C3 have an increase of E_{corr} which levels at ≈ -500 mV for both samples. The cathodic current is also higher at all potentials (more than an order of magnitude at the most negative potentials).¹

Quantitative analysis results of a FFC exposure test are shown in Fig. 8. Considering current industrial requirements and standards (e.g., Qualicoat), the resistance to FFC is sufficient for all the analysed samples even with the weak organic model coating used here. Filament density and the maximum filament length are the two parameters where, albeit small, a difference among the different systems was detected. Both parameters follow a similar trend; the attack is less severe for R than for C3, and less severe for Cu-CC than for model-CC. The increased amount of Cu present in C3 has a slightly negative effect both on the filament density and on the maximum filament length. The slightly negative effect of Cu has also been observed elsewhere [76]. However, the median absolute value is rather high for R's filament density. The high median deviation in filament density for Cu-CC on R shown in Fig. 8 comes from a tested sample that showed an unusual (approximately double) filament density and maximum filament

¹ A fitting of these curves is little meaningful as (a) several curves show very complex shapes beyond simple parametrisation by Tafel slopes and diffusion limited currents, (b) immersion of freshly conversion coated samples as these is not a realistic application, (c) the determination of corrosion current densities in these solutions would be strongly affected by convection, and (d) the uniform corrosion rates of such aluminium alloys are usually less relevant to discuss compared to their localised corrosion propensity.

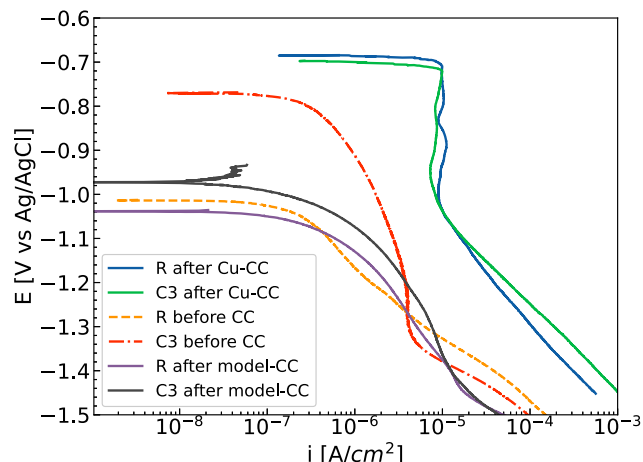


Fig. 7. Cathodic polarisation curves in 5%wt NaCl solution before and after applying Cu-CC, and model-CC.

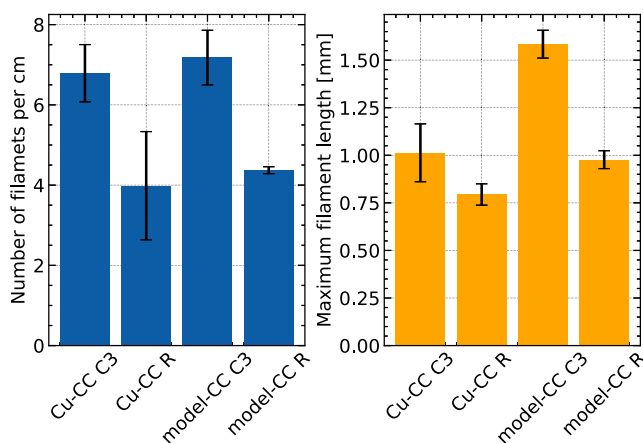


Fig. 8. Median values of filament density and maximum filament length after FFC test for R and C3, conversion coated with model-CC or Cu-CC after application of a weak transparent polyacrylate model organic coating. Error bars represent the median absolute deviation (MAD). MAD represents the median of the absolute deviation of each point from the median.

length. If this sample was not considered the qualitatively observed trend would be even more clear.

4. Discussion

4.1. Interpretation of dEIS results

Before proceeding to a discussion of the chemical processes during CC formation, it is instructive to start with a detailed interpretation of the dEIS results (Fig. 3; Figure S1, Supplementary Material). The observed initial decrease with subsequent slight increase in R_{ct} at constant $E = -0.8$ V could be explained by a two stage mechanism:

1. Predominant deposition of Cu^0 on accessible aluminium; with its active surface, Cu^0 leads to a decrease in R_{ct}
2. After a certain time, the precipitation of ZrO_2 on top of cathodically active sites becomes the predominant process and increases R_{ct}

During the first 25–30 s (not probed by dEIS) the dissolution of the native oxide layer takes place [15,77] and the active aluminium surface becomes exposed to the conversion solution. The deposition of metallic Cu from Cu^{II} is thermodynamically favoured and the process takes place as soon as the native aluminium oxide layer is dissolved. The deposition of particles with better kinetics for the cathodic reactions of oxygen reduction and hydrogen evolution would increase the rate of such reactions and is in agreement with the decrease in R_{ct} during the first ≈ 100 s probed by dEIS. The increased rate of ORR and HER lead to an increase of the local pH which triggers the deposition of ZrO_2 -based products. The deposition of the ZrO_2 -based products takes place initially in close proximity of the noble IMPs [10,15] reducing the surface area available for the ORR and HER. Such a decrease in active area of noble IMPs can account for the increase in R_{ct} observed after 100 s of exposure. In this second phase, the deposition of ZrO_2 -based compounds becomes predominant with respect to the deposition of Cu.

The CPE impedance is defined as

$$Z_{\text{CPE}} = \frac{1}{(j\omega)^\phi Q} \quad (4)$$

The exponent ϕ indicates how far from an ideal capacitive behaviour a certain system is. When $\phi = 1$ the system is an ideal capacitor. The deviation of ϕ from 1 can be attributed to the formation of surface inhomogeneities which can have a parallel or normal distribution with respect to the surface [78].

The change in capacitance (or in Q) reflects the change in the surface oxide properties. The capacitance of a parallel plate capacitor is given as

$$C = \frac{A\epsilon_0\epsilon_{\text{rel}}}{d} \quad (5)$$

where A is the surface area of the plates, ϵ_0 and ϵ_{rel} are the permittivity of free space and the dielectric constant of the material between the plates, respectively, and d is the distance between the parallel plates. Here we assume the metal/solution interfacial region to be in between the two plates. We consider one of the plates of the capacitor to be the metallic surface and the other to be on the outer Helmholtz plane. The capacitor would thus comprehend both the double layer capacitance and the capacitance due to the deposited conversion film. For the deposition and thickening of a surface layer over time a decrease in capacitance could be expected considering the thickness of the depositing layer as the distance d . On the other hand, the deposition of a heterogeneous surface layer would increase the surface area and thus lead to an increase in capacitance.

The constantly decreasing CPE exponent ϕ is in agreement with the increase in capacitance since a decrease in ϕ can be seen as an increase in surface roughness which would lead to an increase in area. Following (5) the variation in area would thus be the factor determining the variation in capacitance. The increase in heterogeneity and thus increase in surface area takes place during the whole conversion process, firstly during the deposition of Cu^0 and secondly during the deposition of ZrO_2 .

Furthermore, the inclusion of water in the depositing conversion layer would also contribute to the increase in capacitance by increasing the global dielectric constant of the system. Such increase in capacitance is usually observed for water uptake in coatings, e.g. [79]. The trend of the fitting parameters such as R_{ct} , Q and ϕ are in line with very recent results presented for a similar conversion system on zinc using operando Odd Random Phase Electrochemical Impedance Spectroscopy [34].

The observed trends in the current (Fig. 3e) imply a capacitive charging of the surface in the initial ≈ 10 s, in agreement with $\phi \approx 1$. The decrease in cathodic current between 50 and 100 s can be understood by a depletion of Cu^{II} near the surface, and a consequent decrease of a diffusion limited deposition current. Subsequently, R_{ct} increases as result of the deposition process by blocking the surface with a high resistance oxide. In the final phase of the deposition, the net

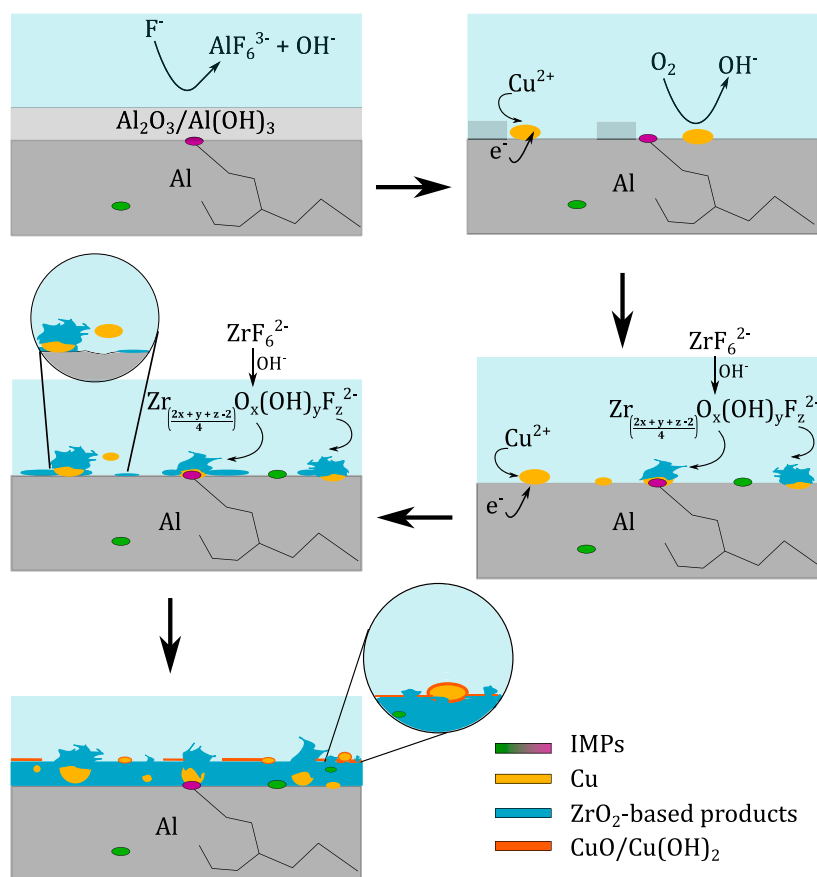


Fig. 9. Proposed deposition mechanism and structure of the forming Cu containing ZrO_2 -based conversion layer. Black lines in the Al region represent selected grain boundaries.

cathodic current increases again, which may be attributed to a decrease in the corresponding anodic dissolution current of aluminium. Overall, the current is also an indication about the distance from the actual OCP at a given time.

The presence of a multi-step deposition mechanism can also be seen from the variation of the R_{ct} with time in the dEIS experiment run during the potential sweep (Figure S1, Supplementary Material). The R_{ct} decreases during the first 100 s in agreement with the deposition of Cu^0 and starts increasing again after 200 s because of the deposition of ZrO_2 -based products partly covering the noble particles. The R_{ct} overall does not change if the value at the beginning and at the end of the measurements is compared. However, potentiodynamic polarisation curves in NaCl shows an enhanced cathodic activity (Fig. 7) so a decrease in R_{ct} should be expected. On the other hand even though on a general level the R_{ct} remains constant, some local areas could be rich in Cu^0 which would explain the enhanced cathodic activity in subsequent polarisation.

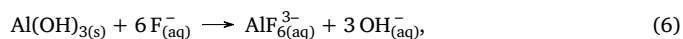
The decrease in capacitance could be explained by the formation of the conversion layer. Even though the capacitance values are in the same range for the experiments run in potentiostatic and potentiodynamic modes, the trend is opposite. The explanation of the observed opposite trend could be different rates of the CC deposition. When kept at a cathodic potential, the deposition of the conversion film is expected to be faster because of the increased rate of local surface alkalinisation favouring the precipitation of ZrO_2 -based compounds following reaction (1). The different deposition rate during the potentiostatic dEIS compared to the potentiodynamic dEIS can be seen from the different times needed by the R_{ct} to start increasing. In this interpretation, the deposition of ZrO_2 -based compounds starts to dominate after ≈ 100 s during the potentiostatic dEIS and after ≈ 200 s during the potentiodynamic EIS. A faster deposition is expected to lead to an increase in

surface roughness, i.e. surface area, which implies an increase of the observed capacitance. Vice versa, during the potentiodynamic dEIS, the Volta potential is slightly below the OCP and the rate of deposition of the CC is lower. The lower deposition rate leads to a better surface homogeneity and the capacitance is expected to decay because of the build-up of a surface layer following Eq. (5) In case of potentiostatic dEIS, the build-up of a surface layer [i.e., increase of d in Eq. (5)] does not dominate the capacitance because of the high increase in surface roughness, (i.e., A dominates the capacitance). The opposite happens during potentiodynamic dEIS.

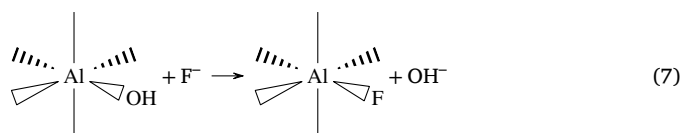
4.2. Formation mechanism ZrO_2 -based conversion coatings

This section will use significant background information from literature for an in-depth discussion of the observations from the experiments conducted in this work.

The first step of CC deposition is a fluoride etching attack on the surface, removing aluminium surface oxide, most likely by the net process of



where $Al(OH)_3$ represents a hydrated surface oxide on aluminium. This process will most likely proceed via a step-wise ligand exchange, represented here schematically for octahedrally coordinated aluminium,



At some stage, the octahedral aluminium hydroxofluorides of type $AlF_x(OH)_{6-x}^{3-}$ become soluble, which leads to a breakdown of the

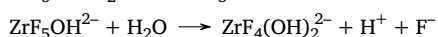
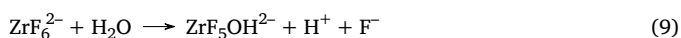
(hydr)oxide and is evidenced by the initially decaying OCP. The changes in OCP are in agreement with previous reports [10,44,80]. A schematic representation is given in the first step of Fig. 9.

The etching chemistry for silicon is expected to have analogies to Al, with the formation of SiF_6^{2-} [81], however, for most other elements, differences are expected, (i) because of the differences in standard potential, and (ii) because of the differences in fluorocomplex formation. Mg and Zn form poorly water soluble fluorides [82]. Mg fluorocomplexes are not water-stable [82]. All the other elements present in larger amounts in the alloy, Cu, Fe, Ni and Mn form fluorocomplexes at sufficiently high fluoride concentrations [82]. The etching properties of the fluoride present in the bath lead to a surface enrichment of the different alloy elements present in the alloy, as shown by GD-OES (Fig. 5). This progressing surface enrichment has consequences on the OCP, which increases in a second stage of the experiments, in line with previous reports [10,44,80].

The second phase of deposition, characterised by an increase in OCP, contains two parallel processes, (i) the deposition of metallic copper and (ii) the precipitation of ZrO_2 . On the free aluminium surface, copper deposition,

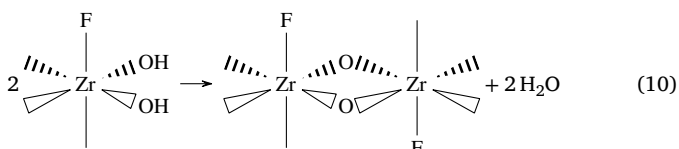


is reflected by the R_{ct} drop. Cu presence is evidenced by GD-OES and the presence of bright spots in SEM and EDX. Noble metal sites are cathodically more active, expected thus to increase hydrogen evolution rates and thus rates of pH increase. As a consequence, they accelerate the hydrolysis of ZrF_6^{2-} which is the equivalent inverse process of the ligand exchange in reaction (7),



:

Hydroxozirconate complexes polymerise in aqueous solution above 100 μM concentration [83]. The formation of tetramers has been found thermodynamically favourable, based on available thermodynamic data [84]. Detailed experimental studies of the zirconate polymerisation in HCl in the pH range 0–3 by electron spray ionisation mass spectrometry show the concurrent presence of species containing 4, 5, 6, 8, 9 and 10 Zr-atoms and the absence of significant amounts of species with lower number of Zr atoms [85,86]. Storage over 2 month led to increasing degree of polymerisation, with 12-mers dominating [85]. At larger pH, further condensation leads to a rich colloidal chemistry of the system [87]. Condensation must schematically proceed via steps such as



with precipitating $\text{ZrO}_{2(s)}$ as final product. Precipitation leads to rising OCP and the change of the surface composition and morphology as discussed in Section 4.1. As expected, Zr is detected in GD-OES and ToF-SIMS on the surfaces. Eq. (10) is again written for octahedrally coordinated Zr, where it is understood that the actual coordination of Zr is supposed to change in the deposition process from octahedral in ZrF_6^{2-} to more complex seven to eightfold in ZrO_2 , based on the structural chemistry of Zr [82, p. 1413–1417]. Incomplete hydrolysis according to reaction (9) leads to the presence of fluoride on the surface, as prominently evidenced in XPS (Fig. 6) and ToF-SIMS (Supplementary Material, Figure S5). The two processes are schematically represented in step 2 and 3 of Fig. 9. Although the two processes must take place simultaneously, following the above reasoning, Cu deposition is predominant in the first phase and the deposition of ZrO_2 -based products dominates in the second phase.

Deposition of both Cu^0 and ZrO_2 takes place predominantly at grain boundaries, to a higher extend on and near IMPs, and to minor degree on the aluminium matrix, which is in line with previous observations [10,12,15,35,88]. The higher OCP of C3 during CC formation could be caused by the higher amount of Cu present in the alloy. The CC deposition also leads to a 5-fold increase in bright particles on C3, compared to doubling on R, and a less pronounced difference in the same direction for the Cu^{II} -free model-CC (Figure S4). On the other hand, GD-OES shows a more than 50-fold increase in copper concentration near the surface after CC formation when comparing Cu^{II} -containing and Cu^{II} -free CC. Compared to the detected surface concentrations of Cu, the effect from the alloy composition on the total Cu concentration on top of the alloy is expected to be minor.

The freshly deposited Cu particles from the Cu-CC are more effective cathodes than the IMPs in the alloy, as evidenced via the distribution of Zr from the EDX measurements (Table 2). In the Cu-CC, there is no increased amount of Zr on the IMPs, as observed for the model-CC. The increased amount of Zr on IMPs can be explained by their cathodic activity, leading to faster increase in pH compared to the surrounding, and consequently preferential deposition of the CC. The absence of this increase indicates that in the Cu-CC, the activity of the freshly deposited Cu leads to deposition of ZrO_2 in other locations, depleting the Zr-containing precursors near the surface and hence suppressing deposition on the IMPs.

4.3. Structure of the formed CCs

There is overwhelming evidence for the co-deposition of Cu^{II} in the final stage of CC formation. First, GD-OES profiles (Fig. 5) show the highest Cu concentration closer to the surface (at ≈ 15 nm depth) than the highest ZrO_2 concentration at ≈ 40 nm. The relative position of the peaks in the GD-OES depth profile might not be very precise due to the surface roughness of the samples or selective sputtering, but similar approaches have been used before in similar systems [43]. Furthermore, also other works found the presence of Cu enrichment on the top of ZrO_2 [50,51] in deposition studies on zinc. Second, ToF-SIMS (Supplementary Material, Figure S5) as very surface-specific method shows the presence of Cu on the surface at least in the investigated intermediate deposition stage. Third, XPS (Fig. 6) shows evidence for the presence of Cu^{II} directly on the surface; similar observations of similar CCs on iron were reported in the literature [37]. Fourth, previous work showed the presence of tenorite CuO [35] or Cu_2O [89] in similar CCs. The reason for the observed co-deposition is the increase in pH during CC deposition (i) through cathodic processes and (ii) through fluoride etching of aluminium oxide [reaction (6)]. Microelectrode measurements have shown pH up to 8.5 in comparable systems during deposition [30]. For the given activity of Cu^{II} , deposition of CuO or $\text{Cu}(\text{OH})_2$ is expected for $\text{pH} > 5.5$ [90].

XPS not only shows the presence of copper hydroxyfluorides in the first few nm of the surface but also reveals that the Cu oxidation state changes with depth starting from a more oxidised form on the top to a less oxidised form at higher depths (Fig. 6c). Judging from both GD-OES profile (Fig. 5; strongest Cu enrichment on the top surface, deposited at later stages at higher pH) and XPS (Fig. 6c), the amount of Cu^{II} supersedes the amount of Cu^0 . The presence of oxidised Cu species could be (i) because of the direct incorporation of Cu^{II} from the CC solution or (ii) the oxidation of deposited Cu^0 . In the latter case, a detachment of metallic Cu particles from the aluminium matrix because of the continuous surface etching caused by fluoride ions is possible. The particles could be oxidised by the presence of dissolved O_2 or NO_3^- ions. The role of the latter has recently been investigated in detail [36]. Considering the presence of different Cu species, hypothesis (ii) is more likely for the largest amount of the detected Cu^{II} , in addition to the directly deposited Cu^{II} on the top surface. However, because of the complex composition and the multitude of chemical

and electrochemical processes possible in the system, it is difficult to conclude on this point with the data collected here.

For what concerns Zr as main indicator for the presence of ZrO_2 , the comparison of the maximum enrichment (≈ 0.7 at.-% for all the curves) and the broadness of the peaks from GD-OES analysis (Fig. 5) suggests that maximum enrichment is independent of the Cu content of the precursor solution. On the other hand, the presence of Cu in the conversion bath favours the increase in thickness of the conversion film, as most obvious from the comparison of the Al and O depth profiles (Fig. 5d). Increased thickness is also evident from the total amount of Zr deposited (broader Zr peak shown in Fig. 5a) and in general from the aluminium profile in Fig. 5d.

The different composition of the two investigated samples also does not have a particular impact on the Zr deposition (Fig. 5a) where the peak representing the Zr enrichment is very similar for the two samples after the application of the CC. EDX (Fig. 4; Table 2) likewise does not show large differences in Zr-content between the different samples. The observed differences in particle counts (Figure S4) therefore does not impact the total Zr amount deposited.

The Cu distribution on the surface after Cu-CC deposition was random from the EDX analysis. Some of the detected bright spots show a very high Cu concentration, whereas Cu is almost absent in other such spots (Fig. 4; Table 2). However, the low lateral resolution of the EDX and its large sampling volume can lead to a high contribution from the matrix and this could superimpose with the signal from surface Cu.

The results from this work do not contradict previous works showing enhanced deposition of ZrO_2 on top of IMPs [10,15,23,88] and deposited Cu^0 [35]. In this work, for Cu-CC, the highest concentration of Cu and Zr was found on the top of IMPs in the grain boundaries. Usually, the ZrO_2 -based compounds tend to precipitate on the top of noble IMPs that increase the local alkalinity which favours the precipitation of ZrO_2 [23]. The presence of elements more noble than Al such as Fe or Mn was found on IMPs all over the alloy matrix but not in the grain boundary regions; these particles instead are Si-rich. The high activity of Si-rich IMPs can be explained by the etching properties of the fluoride-containing conversion bath [81] which result in a dissolution of the surficial SiO_2 and lead to the exposure of the more active Si surface. Cu^0 can then precipitate on the latter increasing the cathodic activity, leading to local alkalisation and favouring the ZrO_2 precipitation. The possibility for Cu^0 particles to precipitate in the CC formation process in the grain boundaries could also explain the reason why a lower amount of Zr is found on the top of the particles in GBs for the model-CC. Thus, Cu^0 has an effect on the distribution of the Zr-based products precipitated from the conversion bath but not on Zr quantity.

The surfaces show enrichment of Ni after CC formation (Fig. 5). Remarkably, the Fe concentration in both R and C3 is similar and higher than the concentration of Ni (Table 1). However, the surface enrichment of Fe is comparable or lower to that of Ni (Fig. 5). Thus, there must be a preferential surface enrichment of the latter. The presence of a surface enrichment of similar magnitude after the deposition of the model-CC suggests that the enrichment is caused by the etching properties of the CC solution, e.g. via dissolution of Ni-containing IMPs and redistribution of the comparably noble Ni.

Ni and Fe as elements less noble than Cu but more noble than Al distribute inside the CCs; there is no sign for enrichment near the metal/CC interface. The peak position of the Ni depth profile correlates well with the one from the Zr profile (Fig. 5). The Fe profile is rather noisy, but its peak is clearly within the CC region. Ni and Fe are furthermore not prominently present in the ToF-SIMS data, but can be detected with certain low intensity in the XPS survey spectra (c.f. Supplementary Material, Figure S9).

4.4. Electrochemical reactivity and corrosion protection mechanism of ZrO_2 -based CCs

Characteristic differences in E_{corr} (Fig. 7) in NaCl solution before CC application can easily be understood based on the different composition of the alloys, as the alloy with higher Cu levels shows a higher E_{corr} . After CC application, differences between the alloys disappeared, so that the conversion treatment determines E_{corr} in both investigated cases.

At sufficiently negative potentials, all polarisation curves show a Tafel-like behaviour, indicating the dominance of the HER at these potentials. Around E_{corr} , the slopes indicate transport control for the Cu-CC which is typically caused by transport-limited ORR, and a mix of transport and activation control for all other samples.

Cathodic activity increases for both samples through the treatment with Cu-CC. The conversion layer deposited from the two baths is similar and it consists of ZrO_2 deposited on the top of noble particles. However, if the noble particles were covered with the same products, an increased electrochemical activity as shown in Fig. 7 should not be expected. This means (under the condition that ZrO_2 deposits on the top of the noble particles) that after the deposition of the Cu-CC, not all the Cu rich particles are covered by the conversion layer; some of them are exposed to the solution during the electrochemical experiments increasing the rate of cathodic reactions such as ORR and HER. Alternatively, some Cu^0 particles lay on the top of the conversion film with conductive paths down to the bulk metal.

In other cases [26,57] the application of a Cu-CC has led to a decrease of the E_{corr} and cathodic activity. However, the increased activity shown in Fig. 7 can be justified by a surface enrichment of Cu deposited from the CC. Such an increase in cathodic activity is not observed after applying the model-CC which did not contain any Cu^{II} additive. Especially in absence of a desmutting step before CC in Ref. [26], because of the presence of Cu rich regions observed by EDX and XPS, the deposited ZrO_2 -based layer was thicker, more uniform, and able to limit the charge transfer, thus lowering the current densities for ORR and HER as shown by polarisation curves [26]. In our case, this decrease in cathodic activity is not observed and for Cu-CC the activity is even higher despite the fact that a thicker oxide layer is found (Fig. 5d).

Cathodic activity at the potentials where HER dominates is little affected by deposition of the model-CC. On the other hand, the reduced E_{corr} observed for C3 can be ascribed to the fact that the noble regions of the surface characterised by high Cu concentration are covered by ZrO_2 -based products during deposition, reducing the nobility of these areas and thus the potential of the interface [10,23].

Larger cathodic activity in potentiodynamic measurements (Fig. 7) and surface enrichment of noble elements that follows the Cu-CC application (Fig. 5) is not reflected in a decreased FFC resistance in the FFC tests (Fig. 8). Consequently, other features of the conversion coating can overcome the possible negative effect of a Cu surface enrichment or a cathodically more active surface. Since FFC is driven by the presence of cathodic IMPs [91], a lower cathodic activity of the surface would be preferred. A reduced cathodic activity after the application of ZrO_2 -based CCs [26,57] has been considered as an indication of an increased corrosion resistance, based on correlation between FFC and cathodic activity [8]. On the other hand, the removal of surficial noble particles on AA6060 reduced their cathodic activity in NaCl solution but did not significantly increase the resistance to FFC because the process is supported by the cathodic activity of the freshly exposed IMPs emerging during the passage of the corrosion front [12]. It has been shown that the CC improves the coating adhesion [12].

The improved resistance of the Cu-CC against FFC could either be attributed to the different distribution of the ZrO_2 , favouring ZrO_2 deposition on the top of non-noble IMPs such as those present in the grain boundaries (Section 3.2.1). Alternatively, the Cu^{II} depositing on the surface could have a role in improved adhesion or FFC resistance.

Independent of the exact mechanism, the potentially negative effect of a high amount of Cu on the surface can be overcome by the beneficial effect of a different conversion film distribution, a thicker conversion film or a better adhesion [12]. Finally, the coating used for this study is a weak model coating chosen in order to observe FFC on the time scales of typical lab experiments, different from industrial grade high performance coatings. Cathodic activity of CC-covered substrates is actually beneficial for some applications such as cathodic electrodeposition coatings; CCs similar to those studies here are themselves stable under cathodic polarisation [45].

It is expected that the presence of residual F-termination and $\text{Cu}(\text{OH})_2$ at the surface improve the adhesion behaviour. Residual fluorides may hydrolyse and be available as fresh reaction sites in coating processes. In aqueous solution, zirconium fluoride species can transform over time to oxidic species during exposure [31]. On the other hand, residual fluoride may increase propensity to oxide damage. Hydroxyl groups are in general important for adhesion of polymers [13, 14].

5. Conclusions

The effect of the nature of the conversion coating and the elemental composition on the electrochemical activity, surface composition, and FFC resistance of a primary and a recycled AA6060 extruded aluminium alloy was investigated.

1. OCP and dEIS during CC formation are determined by an interplay between fluoride induced etching of the aluminium oxide, the deposition of Cu^0 on free aluminium surface, and the formation of ZrO_2 deposits.
2. Cu is found in different forms on the sample surface after the deposition of the Cu-CC. Cu^{II} is found on the top of the ZrO_2 surface while metallic Cu is predominant at greater depths. The largest part of the deposited Cu is most likely the oxidised form. Consequently, these CCs are complex, multielement oxides. This character affects their properties as adhesion promoter and in corrosion protection.
3. The ZrO_2 -based products are differently distributed when two different conversion baths are used. In the case of the Cu-CC, the highest concentration of Zr is found on the top of IMPs precipitated in the grain boundaries while for the model-CC, the concentration of Zr is similar on the top of IMPs precipitated in grain boundaries and in other areas of the surface.
4. The presence of Cu^{II} in the conversion bath increases the cathodic activity of the surface because of a deposition of cathodically active, noble Cu^0 . This allows the formation of a ≈ 30 nm thicker conversion layer and a different distribution of the precipitated ZrO_2 -based products when comparing to Cu^{II} -free systems. Nevertheless, the maximum surface concentration of Zr is similar for both Cu^{II} -free and Cu^{II} -containing CC.
5. Increasing the amount of Cu in the alloy from ≈ 30 ppm to ≈ 300 ppm has a slightly negative effect on both filament density and maximum filament length, with differences of several ten percent, as shown by FFC tests. Despite the fact that the Cu-CC shows a ca. order of magnitude higher cathodic activity, its performance in the FFC tests is slightly superior to that of model-CC. Overall, both samples and conversion systems show a maximum filament length in the range 0.8–1.55 mm.
6. Although a difference in electrochemical activity was observed before the application of a conversion layer, no substantial difference in FFC resistance has been evidenced between recycled and primary alloys after conversion coating.

CRediT authorship contribution statement

Erlind Mysliu: Data curation, Formal analysis, Investigation, Methodology, Visualization, Writing – original draft, Writing – review & editing. **Kathrine Sletteberg Storli:** Formal analysis, Investigation. **Hanna Marie Skogøy:** Formal analysis, Investigation. **Stephan Kubowicz:** Investigation, Writing – review & editing. **Ingeborg-Helene Svenum:** Data curation, Formal analysis, Investigation, Writing – review & editing. **Otto Lunder:** Conceptualization, Funding acquisition, Methodology, Supervision, Writing – review & editing. **Andreas Erbe:** Conceptualization, Funding acquisition, Methodology, Supervision, Writing – original draft, Writing – review & editing.

Declaration of competing interest

The authors declare the following financial interests/personal relationships which may be considered as potential competing interests: S.K., I.-H.S., O.L. and A.E. have a wide academic and industrial network and a number of research activities beyond this manuscript which may be related to the topic to a certain degree.

Data availability

Research data produced in relation to this work is available at NTNU Open Research Data, <https://doi.org/10.18710/DYRRAE>.

Acknowledgements

This work was part of the project “Coated Recycled Aluminium - developing surfaces for well-adhering and corrosion resistant coating systems” supported by the Research Council of Norway (No. 309875), Hydro and Speira. The authors would also like to thank Thomas Holm for his help and discussions about the technical details of the dEIS set-up. Jan Tore Buvik Gundersen is acknowledged for discussions on GD-OES analysis, Malgorzata Halseid for management support and Anita Storsve for technical support.

Appendix A. Supplementary data

Supplementary material related to this article can be found online at <https://doi.org/10.1016/j.electacta.2024.143805>.

References

- [1] European Aluminium, Environmental Profile Report for the Aluminium Refining Industry, Tech. rep., Bruxelles, Belgium, 2022, URL <https://european-aluminium.eu/blog/environmental-profile-reports/>. Accessed 05 May 2023.
- [2] S. Tjøtta, L. Dardinier, B. Kurth, High quality extrusion billets made from post-consumer scrap, *Alum. Extrus. Finish.* (2020) 18–24.
- [3] N. Birbilis, R.G. Buchheit, Electrochemical characteristics of intermetallic phases in aluminum alloys: An experimental survey and discussion, *J. Electrochem. Soc.* 152 (4) (2005) B140, <http://dx.doi.org/10.1149/1.1869984>.
- [4] E. Mysliu, O. Lunder, A. Erbe, Role of aluminium hydrides in localised corrosion of aluminium revealed by operando Raman spectroscopy, *Phys. Chem. Phys.* 25 (2023) 11845–11857, <http://dx.doi.org/10.1039/D3CP00522D>.
- [5] X. Zhou, G. Thompson, G. Scamans, The influence of surface treatment on filiform corrosion resistance of painted aluminium alloy sheet, *Corros. Sci.* 45 (8) (2003) 1767–1777, [http://dx.doi.org/10.1016/S0010-938X\(03\)00003-9](http://dx.doi.org/10.1016/S0010-938X(03)00003-9).
- [6] A. Afseth, J. Nordlien, G. Scamans, K. Nisançioğlu, Effect of heat treatment on filiform corrosion of aluminium alloy AA3005, *Corros. Sci.* 43 (11) (2001) 2093–2109, [http://dx.doi.org/10.1016/S0010-938X\(01\)00014-2](http://dx.doi.org/10.1016/S0010-938X(01)00014-2).
- [7] H. Leth-Olsen, A. Afseth, K. Nisançioğlu, Filiform corrosion of aluminium sheet. II. Electrochemical and corrosion behaviour of bare substrates, *Corros. Sci.* 40 (7) (1998) 1195–1214, [http://dx.doi.org/10.1016/S0010-938X\(98\)00025-0](http://dx.doi.org/10.1016/S0010-938X(98)00025-0).
- [8] A. Afseth, J. Nordlien, G. Scamans, K. Nisançioğlu, Effect of thermo-mechanical processing on filiform corrosion of aluminium alloy AA3005, *Corros. Sci.* 44 (11) (2002) 2491–2506, [http://dx.doi.org/10.1016/S0010-938X\(02\)00036-7](http://dx.doi.org/10.1016/S0010-938X(02)00036-7).
- [9] H. Leth-Olsen, K. Nisançioğlu, Filiform corrosion of aluminium sheet. I. Corrosion behaviour of painted material, *Corros. Sci.* 40 (7) (1998) 1179–1194, [http://dx.doi.org/10.1016/S0010-938X\(98\)00026-2](http://dx.doi.org/10.1016/S0010-938X(98)00026-2).

- [10] F. Andreatta, A. Turco, I. de Graeve, H. Terryn, J. de Wit, L. Fedrizzi, SKPFM and SEM study of the deposition mechanism of Zr/Ti based pre-treatment on AA6016 aluminum alloy, *Surf. Coat. Technol.* 201 (18) (2007) 7668–7685, <http://dx.doi.org/10.1016/j.surfcoat.2007.02.039>.
- [11] N. Le Bozec, S. Joiret, D. Thierry, D. Persson, The role of chromate conversion coating in the filiform corrosion of coated aluminum alloys, *J. Electrochem. Soc.* 150 (12) (2003) B561, <http://dx.doi.org/10.1149/1.1621413>.
- [12] O. Lunder, K.F. Heen, K. Nisançioğlu, Pretreatment of Aluminum Alloy 6060 by Selective Removal of Surface Intermetallics, *Corrosion* 60 (7) (2004) 622–631, <http://dx.doi.org/10.5006/1.3287837>.
- [13] L. Fockaert, S. Pletincx, D. Ganzinga-Jurg, B. Boelen, T. Hauffman, H. Terryn, J. Mol, Chemisorption of polyester coatings on zirconium-based conversion coated multi-metal substrates and their stability in aqueous environment, *Appl. Surf. Sci.* 508 (2020) 144771, <http://dx.doi.org/10.1016/j.apsusc.2019.144771>.
- [14] E. Ramanathan, S. Balasubramanian, Comparative study on polyester epoxy powder coat and amide cured epoxy liquid paint over nano-zirconia treated mild steel, *Prog. Org. Coat.* 93 (2016) 68–76, <http://dx.doi.org/10.1016/j.porgcoat.2016.01.007>.
- [15] O. Lunder, C. Simensen, Y. Yu, K. Nisançioğlu, Formation and characterisation of Ti–Zr based conversion layers on AA6060 aluminium, *Surf. Coat. Technol.* 184 (2) (2004) 278–290, <http://dx.doi.org/10.1016/j.surfcoat.2003.11.003>.
- [16] M.-G. Olivier, M. Poelman, M. Demuynek, J.-P. Petitjean, EIS evaluation of the filiform corrosion of aluminium coated by a cathodic paint, *Prog. Org. Coat.* 52 (4) (2005) 263–270, <http://dx.doi.org/10.1016/j.porgcoat.2004.05.008>.
- [17] A. Nazarov, A.-P. Romano, M. Fedel, F. Deflorian, D. Thierry, M.-G. Olivier, Filiform corrosion of electrocoated aluminium alloy: Role of surface pretreatment, *Corros. Sci.* 65 (2012) 187–198, <http://dx.doi.org/10.1016/j.corsci.2012.08.013>.
- [18] D. Iqbal, J. Rechmann, A. Sarfraz, A. Altin, G. Genchev, A. Erbe, Synthesis of ultrathin poly(methyl methacrylate) model coatings bound via organosilanes to zinc and investigation of their delamination kinetics, *ACS Appl. Mater. Interfaces* 6 (20) (2014) 18112–18121, <http://dx.doi.org/10.1021/am504992r>.
- [19] C. Fernández-Solis, A. Erbe, Waterborne chitosan–epoxysilane hybrid pretreatments for corrosion protection of zinc, *Biointerphases* 11 (2) (2016) 021001, <http://dx.doi.org/10.1116/1.4944828>.
- [20] C. Fernández-Solis, P. Keil, A. Erbe, Molybdate and phosphate cross-linked chitosan films for corrosion protection of hot-dip galvanized steel, *ACS Omega* 8 (22) (2023) 19613–19624, <http://dx.doi.org/10.1021/acsomega.3c01119>.
- [21] M. Fedel, C. Zanella, L. Ferrari, F. Deflorian, Effect of the synthesis parameters of in situ grown Mg–Al LDHs on the filiform corrosion susceptibility of painted AA5005, *Electrochim. Acta* 381 (2021) 138288, <http://dx.doi.org/10.1016/j.electacta.2021.138288>.
- [22] I. Milošev, G.S. Frankel, Review—Conversion coatings based on Zirconium and/or Titanium, *J. Electrochem. Soc.* 165 (3) (2018) C127, <http://dx.doi.org/10.1149/2.0371803jes>.
- [23] J. Nordlien, J. Walmsley, H. Østerberg, K. Nisançioğlu, Formation of a zirconium-titanium based conversion layer on AA 6060 aluminium, *Surf. Coat. Technol.* 153 (1) (2002) 72–78, [http://dx.doi.org/10.1016/S0257-8972\(01\)01663-2](http://dx.doi.org/10.1016/S0257-8972(01)01663-2).
- [24] S. Adhikari, K. Unocic, Y. Zhai, G. Frankel, J. Zimmerman, W. Frisdat, Hexafluoro-zirconic acid based surface pretreatments: Characterization and performance assessment, *Electrochim. Acta* 56 (4) (2011) 1912–1924, <http://dx.doi.org/10.1016/j.electacta.2010.07.037>.
- [25] A. Adediran, M. Oki, S. Akintola, B. Ogunsemi, E. Akinlabi, Electron-optical and Auger electron spectroscopy studies of a zirconium conversion coating on aluminium, *Mater. Tehnol.* 53 (2019) 183–188, <http://dx.doi.org/10.17222/mit.2018.197>.
- [26] C. Glover, M. Lim, J. Scully, Increased filiform corrosion resistance utilizing a zirconium-based conversion coating on an Al–Zn–Mg–Cu (AA7075–T6) alloy as well as selected surface treatments, *Corrosion* 77 (1) (2020) 40–52, <http://dx.doi.org/10.5006/3510>.
- [27] V. Cristaudo, K. Baert, P. Laha, M. Lyn Lim, E. Brown-Tseng, H. Terryn, T. Hauffman, A combined XPS/ToF-SIMS approach for the 3D compositional characterization of Zr-based conversion of galvanized steel, *Appl. Surf. Sci.* 562 (2021) 150166, <http://dx.doi.org/10.1016/j.apsusc.2021.150166>.
- [28] A.V. Rudakova, A.V. Emeline, K.M. Bulanin, L.V. Chistyakova, M.V. Maevskaya, D.W. Bahnemann, Self-cleaning properties of zirconium dioxide thin films, *J. Photochem. Photobiol. A* 367 (2018) 397–405, <http://dx.doi.org/10.1016/j.jphotochem.2018.08.037>.
- [29] G. Šekularac, J. Kovač, I. Milošev, Comparison of the electrochemical behaviour and self-sealing of zirconium conversion coatings applied on aluminium alloys of series 1xxx to 7xxx, *J. Electrochem. Soc.* 167 (11) (2020) 111506, <http://dx.doi.org/10.1149/1945-7111/aba875>.
- [30] L. Li, A.L. Desouza, G.M. Swain, In situ pH measurement during the formation of conversion coatings on an aluminium alloy (AA2024), *Analyst* 138 (2013) 4398–4402, <http://dx.doi.org/10.1039/C3AN00663H>.
- [31] G. Šekularac, J. Kovač, I. Milošev, Prolonged protection, by zirconium conversion coatings, of AlSi7Mg0.3 aluminium alloy in chloride solution, *Corros. Sci.* 169 (2020) 108615, <http://dx.doi.org/10.1016/j.corsci.2020.108615>.
- [32] G. Šekularac, I. Milošev, Electrochemical behavior and self-sealing ability of zirconium conversion coating applied on aluminum alloy 3005 in 0.5 M NaCl solution, *J. Electrochem. Soc.* 167 (2) (2020) 021509, <http://dx.doi.org/10.1149/1945-7111/ab6b0d>.
- [33] M. Mujdrica Kim, B. Kapun, U. Tiringner, G. Šekularac, I. Milošev, Protection of aluminum alloy 3003 in sodium chloride and simulated acid rain solutions by commercial conversion coatings containing Zr and Cr, *Coatings* 9 (9) (2019) <http://dx.doi.org/10.3390/coatings9090563>.
- [34] M. Dabiri Havigh, M. Nabizadeh, B. Wouters, N. Hallemans, T. Hauffman, J. Lataire, A. Hubin, H. Terryn, Operando odd random phase electrochemical impedance spectroscopy (ORP-EIS) for in-situ monitoring of the Zr-based conversion coating growth in the presence of (in)organic additives, *Corros. Sci.* 223 (2023) 111469, <http://dx.doi.org/10.1016/j.corsci.2023.111469>.
- [35] A. Sarfraz, R. Posner, M.M. Lange, K. Lill, A. Erbe, Role of intermetallics and copper in the deposition of ZrO₂ conversion coatings on AA6014, *J. Electrochem. Soc.* 161 (12) (2014) C509, <http://dx.doi.org/10.1149/2.0121412jes>.
- [36] J. Han, D. Thierry, K. Ogle, Zr-based conversion coating on Zn and Zn–Al–Mg alloy coating: Understanding the accelerating effect of Cu(II) and NO₃⁻, *Surf. Coat. Technol.* 402 (2020) 126236, <http://dx.doi.org/10.1016/j.surfcoat.2020.126236>.
- [37] X. Liu, D. Vonk, K. Kisslinger, X. Tong, G. Halada, S. Petrasch, K. Foster, Y.-c.K. Chen-Wiegart, Unraveling the formation mechanism of a hybrid Zr-based chemical conversion coating with organic and copper compounds for corrosion inhibition, *ACS Appl. Mater. Interfaces* 13 (4) (2021) 5518–5528, <http://dx.doi.org/10.1021/acami.0c19203>.
- [38] J. Cerezo, I. Vandendael, R. Posner, K. Lill, J. de Wit, J. Mol, H. Terryn, Initiation and growth of modified Zr-based conversion coatings on multi-metal surfaces, *Surf. Coat. Technol.* 236 (2013) 284–289, <http://dx.doi.org/10.1016/j.surfcoat.2013.09.059>.
- [39] J. Cerezo, I. Vandendael, R. Posner, J. de Wit, J. Mol, H. Terryn, The effect of surface pre-conditioning treatments on the local composition of Zr-based conversion coatings formed on aluminium alloys, *Appl. Surf. Sci.* 366 (2016) 339–347, <http://dx.doi.org/10.1016/j.apsusc.2016.01.106>.
- [40] J. Cerezo, P. Taheri, I. Vandendael, R. Posner, K. Lill, J. de Wit, J. Mol, H. Terryn, Influence of surface hydroxyls on the formation of Zr-based conversion coatings on AA6014 aluminum alloy, *Surf. Coat. Technol.* 254 (2014) 277–283, <http://dx.doi.org/10.1016/j.surfcoat.2014.06.030>.
- [41] W. Zhan, X. Qian, B. Gui, L. Liu, X. Liu, Z. Li, L. Hu, Preparation and corrosion resistance of titanium–zirconium–cerium based conversion coating on 6061 aluminum alloy, *Mater. Corros.* 71 (3) (2020) 419–429, <http://dx.doi.org/10.1002/maco.201911193>.
- [42] F. George, P. Skeldon, G. Thompson, Formation of zirconium-based conversion coatings on aluminium and Al–Cu alloys, *Corros. Sci.* 65 (2012) 231–237, <http://dx.doi.org/10.1016/j.corsci.2012.08.031>.
- [43] F. Andreatta, A. Lanzutti, L. Paussa, L. Fedrizzi, Addition of phosphates or copper nitrate in a fluotitanate conversion coating containing a silane coupling agent for aluminium alloy AA6014, *Prog. Org. Coat.* 77 (12, Part B) (2014) 2107–2115, <http://dx.doi.org/10.1016/j.porgcoat.2014.05.020>.
- [44] T. Lostak, S. Krebs, A. Maljusch, T. Gothe, M. Giza, M. Kimpel, J. Flock, S. Schulz, Formation and characterization of Fe³⁺/Cu²⁺-modified zirconium oxide conversion layers on zinc alloy coated steel sheets, *Electrochim. Acta* 112 (2013) 14–23, <http://dx.doi.org/10.1016/j.electacta.2013.08.161>.
- [45] A. Sarfraz, R. Posner, A. Bashir, A. Topalov, K.J.J. Mayrhofer, K. Lill, A. Erbe, Effect of polarisation mimicking cathodic electrodeposition coating on industrially relevant metal substrates with ZrO₂-based conversion coatings, *ChemElectroChem* 3 (9) (2016) 1415–1421, <http://dx.doi.org/10.1002/celec.201600216>.
- [46] T. Lostak, C. Timma, S. Krebs, J. Flock, S. Schulz, Organosilane modified Zr-based conversion layer on Zn–Al alloy coated steel sheets, *Surf. Coat. Technol.* 305 (2016) 223–230, <http://dx.doi.org/10.1016/j.surfcoat.2016.08.030>.
- [47] J.S. Mondragón-Ochoa, A. Altin, J. Rechmann, A. Erbe, Delamination kinetics of thin film poly(acrylate) model coatings prepared by surface initiated atom transfer radical polymerization on iron, *J. Electrochem. Soc.* 165 (16) (2018) C991, <http://dx.doi.org/10.1149/2.0241816jes>.
- [48] D. Iqbal, J. Rechmann, A. Bashir, A. Sarfraz, A. Altin, A. Erbe, Cathodic delamination kinetics of thin polystyrene model coatings bound to zinc via organosilanes, *Mater. Corros.* 70 (3) (2019) 481–491, <http://dx.doi.org/10.1002/maco.201810395>.
- [49] X. Zuo, W. Li, S. Mu, J. Du, Y. Yang, P. Tang, Investigation of composition and structure for a novel Ti–Zr chemical conversion coating on 6063 aluminum alloy, *Prog. Org. Coat.* 87 (2015) 61–68, <http://dx.doi.org/10.1016/j.porgcoat.2015.05.008>.
- [50] M. Nabizadeh, K. Marcoen, E.A. Mernissi Cherigui, T. Kolberg, D. Schatz, H. Terryn, T. Hauffman, Unraveling the formation mechanism of hybrid Zr conversion coating on advanced high strength stainless steels, *Surf. Coat. Technol.* 441 (2022) 128567, <http://dx.doi.org/10.1016/j.surfcoat.2022.128567>.
- [51] M. Nabizadeh, K. Marcoen, E. Amine Mernissi Cherigui, M. Dabiri Havigh, T. Kolberg, D. Schatz, H. Terryn, T. Hauffman, Investigation of hybrid Zr-aminosilane treatment formation on zinc substrate and comparison to advanced high strength stainless steel, *Appl. Surf. Sci.* 610 (2023) 155554, <http://dx.doi.org/10.1016/j.apsusc.2022.155554>.
- [52] L. Fockaert, M. Ankora, J. Van Dam, S. Pletincx, A. Yilmaz, B. Boelen, T. Hauffman, Y. Garcia-Gonzalez, H. Terryn, J. Mol, Effect of organic additives in fluoacid-based Ti and Zr-treatments for galvanized steel on the stability of a polymer coated interface, *Prog. Org. Coat.* 146 (2020) 105738, <http://dx.doi.org/10.1016/j.porgcoat.2020.105738>.

- [53] R.K. Suleiman, A.M. Kumar, M.M. Rahman, F.A. Al-Badour, M.H. Meliani, T.A. Saleh, Effect of metal oxide additives on the structural and barrier properties of a hybrid organosilicon sol-gel coating in 3.5% NaCl medium, *Prog. Org. Coat.* 148 (2020) 105825, <http://dx.doi.org/10.1016/j.porgcoat.2020.105825>.
- [54] J. Qi, T. Hashimoto, J. Walton, X. Zhou, P. Skeldon, G.E. Thompson, Formation of a trivalent chromium conversion coating on AA2024-T351 alloy, *J. Electrochem. Soc.* 163 (2) (2015) C25, <http://dx.doi.org/10.1149/2.0771602jes>.
- [55] E. Mysliu, K. Sletteberg Storli, E. Kjorsvik, O. Lunder, A. Erbe, Recycled aluminium alloys and their models: Role and behaviour of alloying elements during alkaline etching, *J. Electrochem. Soc.* 170 (1) (2023) 011503, <http://dx.doi.org/10.1149/1945-7111/acb38a>.
- [56] C. Glover, M. Lim, G. Post, M. Mayo, J. Scully, The effect of surface treatment on the performance of a trivalent chromium process (TCP) pretreatment on AA7075 aerospace alloys for the protection against filiform corrosion, *Corrosion* 75 (12) (2019) 1513–1526, <http://dx.doi.org/10.5006/3380>.
- [57] Y. Liu, Y. Yang, C. Zhang, T. Zhang, B. Yu, G. Meng, Y. Shao, F. Wang, L. Liu, Protection of AA5083 by a zirconium-based conversion coating, *J. Electrochem. Soc.* 163 (9) (2016) C576, <http://dx.doi.org/10.1149/2.1021609jes>.
- [58] P. Zhou, Y. Liu, L. Liu, B. Yu, T. Zhang, F. Wang, Critical role of pretreatment on the corrosion resistance of Zr conversion coating on 6061 aluminum alloy: The combined effect of surface topography and potential difference between different phases, *Surf. Coat. Technol.* 377 (2019) 124904, <http://dx.doi.org/10.1016/j.surfcoat.2019.124904>.
- [59] E. Mysliu, K. Sletteberg Storli, H.M. Skogoy, S. Kubowicz, L.-H. Svenum, O. Lunder, A. Erbe, Replication data for: "Effect of Cu²⁺ on deposition mechanism and structure of ZrO₂-based conversion coatings on AA6060 aluminium alloys and their susceptibility to filiform corrosion", 2023, NTNU Open Research Data, <https://doi.org/10.18710/DYRRAE>.
- [60] R.L. Sacci, D. Harrington, Dynamic electrochemical impedance spectroscopy, *ECS Trans.* 19 (20) (2009) 31, <http://dx.doi.org/10.1149/1.3247564>.
- [61] G.S. Popkirk, R.N. Schindler, Optimization of the perturbation signal for electrochemical impedance spectroscopy in the time domain, *Rev. Sci. Instrum.* 64 (11) (1993) 3111–3115, <http://dx.doi.org/10.1063/1.1144316>.
- [62] M.D. Murbach, B. Gerwe, N. Dawson-Elli, L.-k. Tsui, impedance.py: A python package for electrochemical impedance analysis, *J. Open Source Softw.* 5 (52) (2020) 2349, <http://dx.doi.org/10.21105/joss.02349>.
- [63] C.H. Hsu, F. Mansfeld, Technical note: Concerning the conversion of the constant phase element parameter Y₀ into a capacitance, *Corrosion* 57 (9) (2001) 747–748, <http://dx.doi.org/10.5006/1.3280607>.
- [64] A. Lasia, The origin of the constant phase element, *J. Phys. Chem. Lett.* 13 (2) (2022) 580–589, <http://dx.doi.org/10.1021/acs.jpcclett.1c03782>.
- [65] S.P. Harrington, T.M. Devine, Analysis of electrodes displaying frequency dispersion in mott-schottky tests, *J. Electrochem. Soc.* 155 (8) (2008) C381, <http://dx.doi.org/10.1149/1.2929819>.
- [66] C.A. Schneider, W.S. Rasband, K.W. Eliceiri, NIH Image to ImageJ: 25 years of image analysis, *Nature Methods* 5 (52) (2012) 671–675, <http://dx.doi.org/10.1038/nmeth.2089>.
- [67] N. Kuijpers, W. Kool, P. Koenis, K. Nilsen, I. Todd, S. van der Zwaag, Assessment of different techniques for quantification of α -Al(FeMn)Si and β -AlFeSi intermetallics in AA 6xxx alloys, *Mater. Charact.* 49 (5) (2002) 409–420, [http://dx.doi.org/10.1016/S1044-5803\(03\)00036-6](http://dx.doi.org/10.1016/S1044-5803(03)00036-6).
- [68] Y. Birol, Homogenization of EN AW 6005A alloy for improved extrudability, *Metall. Mater. Trans. A* 44 (1) (2013) 504–511, <http://dx.doi.org/10.1007/s11661-012-1379-y>.
- [69] L. Lodgaard, N. Ryum, Precipitation of dispersoids containing Mn and/or Cr in Al–Mg–Si alloys, *Mater. Sci. Eng. A* 283 (1) (2000) 144–152, [http://dx.doi.org/10.1016/S0921-5093\(00\)00734-6](http://dx.doi.org/10.1016/S0921-5093(00)00734-6).
- [70] Y. Wu, J. Xiong, R. Lai, X. Zhang, Z. Guo, The microstructure evolution of an Al–Mg–Si–Mn–Cu–Ce alloy during homogenization, *J. Alloys Compd.* 475 (1) (2009) 332–338, <http://dx.doi.org/10.1016/j.jallcom.2008.07.032>.
- [71] M.C. Biesinger, Advanced analysis of copper X-ray photoelectron spectra, *Surf. Interface Anal.* 49 (13) (2017) 1325–1334, <http://dx.doi.org/10.1002/sia.6239>.
- [72] A.V. Naumkin, A. Kraut-Vass, S.W. Gaarenstroom, C.J. Powell, NIST X-ray photoelectron spectroscopy database 20, version 4.1, 2012, <http://dx.doi.org/10.18434/T4T88K>, URL <https://srdata.nist.gov/xps/>.
- [73] M. Mosafiri, P. Selles, T. Miteva, A. Ferté, S. Carniato, Interpretation of shakeup mechanisms in copper L-shell photoelectron spectra, *J. Phys. Chem. A* 126 (30) (2022) 4902–4914, <http://dx.doi.org/10.1021/acs.jpca.2c01870>.
- [74] Z.-X. Shen, R.S. List, D.S. Dessau, F. Parmigiani, A.J. Arko, R. Bartlett, B.O. Wells, I. Lindau, W.E. Spicer, Photoemission study of CuO and Cu₂O single crystals, *Phys. Rev. B* 42 (1990) 8081–8085, <http://dx.doi.org/10.1103/PhysRevB.42.8081>.
- [75] C. Toparli, A. Sarfraz, A. Erbe, A new look at oxide formation at the copper/electrolyte interface by in situ spectroscopies, *Phys. Chem. Chem. Phys.* 17 (2015) 31670–31679, <http://dx.doi.org/10.1039/C5CP05172J>.
- [76] A. Lutz, M. Chojak Halseid, I. De Graeve, Corrosion performance of powder-coated aluminum profiles with increased trace element content, *Mater. Corros.* 73 (10) (2022) 1575–1585, <http://dx.doi.org/10.1002/maco.202213173>.
- [77] S.S. Golru, M. Attar, B. Ramezanzadeh, Morphological analysis and corrosion performance of zirconium based conversion coating on the aluminum alloy 1050, *J. Ind. Eng. Chem.* 24 (2015) 233–244, <http://dx.doi.org/10.1016/j.jiec.2014.09.036>.
- [78] B. Hirschorn, M.E. Orazem, B. Tribollet, V. Vivier, I. Frateur, M. Musiani, Determination of effective capacitance and film thickness from constant-phase-element parameters, *Electrochim. Acta* 55 (21) (2010) 6218–6227, <http://dx.doi.org/10.1016/j.electacta.2009.10.065>.
- [79] C.D. Fernández-Solis, A. Vimalanandan, A. Altin, J.S. Mondragón-Ochoa, K. Kreth, P. Keil, A. Erbe, Fundamentals of electrochemistry, corrosion and corrosion protection, in: P.R. Lang, Y. Liu (Eds.), *Soft Matter At Aqueous Interfaces*, in: *Lect. Notes Phys.*, vol. 917, Springer, Cham, Switzerland, 2016, pp. 29–70, http://dx.doi.org/10.1007/978-3-319-24502-7_2.
- [80] I. Schoukens, I. Vandendael, J. De Strycker, A.A. Saleh, H. Terryn, I. De Graeve, Effect of surface composition and microstructure of aluminised steel on the formation of a titanium-based conversion layer, *Surf. Coat. Technol.* 235 (2013) 628–636, <http://dx.doi.org/10.1016/j.surfcoat.2013.08.041>.
- [81] P. Schneider, R. Sigel, M.M. Lange, F. Beier, F.U. Renner, A. Erbe, Activation and fluoride-assisted phosphating of aluminum-silicon-coated steel, *ACS Appl. Mater. Interfaces* 5 (10) (2013) 4224–4232, <http://dx.doi.org/10.1021/am400409k>.
- [82] N. Wiberg, *Holleman-Wiberg - Lehrbuch Der Anorganischen Chemie, 101st ed.*, Walter de Gruyter, Berlin, 1995.
- [83] C.F. Baes Jr., R.E. Mesmer, *The Hydrolysis of Cations*, Wiley Interscience, New York, 1976, pp. 152–158.
- [84] A. Kraš, I. Milošev, The aqueous chemistry of zirconium as a basis for better understanding the formation of zirconium conversion coatings: Updated thermodynamic data, *J. Electrochem. Soc.* 170 (2) (2023) 021508, <http://dx.doi.org/10.1149/1945-7111/acb9c2>.
- [85] T. Sasaki, O. Nakaoka, R. Arakawa, T. Kobayashi, I. Takagi, H. Moriyama, Detection of polynuclear zirconium hydroxide species in aqueous solution by desktop ESI-MS, *J. Nucl. Sci. Technol.* 47 (12) (2010) 1211–1218, <http://dx.doi.org/10.1080/18811248.2010.972098>.
- [86] C. Walther, J. Rothe, M. Fuss, S. Büchner, S. Koltsov, T. Bergmann, Investigation of polynuclear Zr(IV) hydroxide complexes by nanoelectrospray mass-spectrometry combined with XAFS, *Anal. Bioanal. Chem.* 388 (2) (2007) 409–431, <http://dx.doi.org/10.1007/s00216-007-1223-1>.
- [87] H. Cölfen, H. Schnablegger, A. Fischer, F.C. Jentoft, G. Weinberg, R. Schlögl, Particle growth kinetics in zirconium sulfate aqueous solutions followed by dynamic light scattering and analytical ultracentrifugation: Implications for thin film deposition, *Langmuir* 18 (9) (2002) 3500–3509, <http://dx.doi.org/10.1021/la0116286>.
- [88] P. Bouckennoog, O. Bauer, K. Eckhard, H. Terryn, On the use of AES data analysis to determine local enrichments of conversion coating elements at intermetallic particles on rolled Al, *Surf. Interface Anal.* 52 (4) (2020) 174–184, <http://dx.doi.org/10.1002/sia.6738>.
- [89] X. Liu, D. Vonk, H. Jiang, K. Kisslinger, X. Tong, M. Ge, E. Nazaretski, B. Ravel, K. Foster, S. Petrash, Y.-c.K. Chen-Wiegart, Environmentally friendly Zr-based conversion nanocoatings for corrosion inhibition of metal surfaces evaluated by multimodal X-ray analysis, *ACS Appl. Nano Mater.* 2 (4) (2019) 1920–1929, <http://dx.doi.org/10.1021/acsnm.8b02309>.
- [90] N. de Zoubov, C. Vanleugenhaghe, M. Pourbaix, in: M. Pourbaix (Ed.), *Atlas of Electrochemical Equilibria in Aqueous Solutions*, National Association of Corrosion Engineers / Centre Belge d'Etude de la Corrosion CEBELCOR, Houston / Bruxelles, 1974, pp. 384–392.
- [91] C. Senöz, M. Rohwerder, Scanning Kelvin probe force microscopy for the in situ observation of the direct interaction between active head and intermetallic particles in filiform corrosion on aluminium alloy, *Electrochim. Acta* 56 (26) (2011) 9588–9595, <http://dx.doi.org/10.1016/j.electacta.2011.02.052>.